

An immersed boundary method for the discrete velocity model of the Boltzmann equation

Longqing Ge^a, Qingdong Cai^a, Yonghao Zhang^{b,c}, Tianbai Xiao^{b,c,*}

^a*Department of Mechanics, School of Mechanics and Engineering Science, Peking University, Beijing, China*

^b*Centre for Interdisciplinary Research in Fluids, Institute of Mechanics, Chinese Academy of Sciences, Beijing, China*

^c*School of Engineering Science, University of Chinese Academy of Sciences, Beijing, China*

Abstract

Computational modeling and simulation of fluid-structure interactions constitute a fundamental cornerstone for advancing aerospace engineering endeavors. This paper addresses the notion and implementation of the immersed boundary method for the discrete velocity model of the Boltzmann equation. The method incorporates the Maxwell gas–surface interaction model into the construction of ghost-cell particle distribution functions, facilitating meticulous characterization of velocity slip and temperature jump effects within a Cartesian grid framework, which ultimately achieves accurate prediction of aerodynamic parameters. This study presents two principal advancements. First, an upwind-weighted compact interpolation strategy is developed in physical space, which ensures numerical stability and robustness for arbitrary geometries without relying on large stencils or normal-direction projections. Second, a cut-cell correction methodology is proposed in velocity space to address the degradation of quadrature accuracy caused by surface discontinuities. The resulting framework is equally applicable to both two- and three-dimensional problems without requiring any dimension-specific modifications. Rigorous analysis is provided to prove that the approach maintains second-order accuracy across both physical and velocity space, while ensuring robust numerical stability. Comprehensive numerical experiments demonstrate that the solution algorithm achieves the designed accuracy and delivers precise predictions comparable to body-conformal solvers, while retaining the simplicity, flexibility, and scalability of the Cartesian grid method. The proposed approach provides a unified and physically consistent immersed boundary framework for simulating dynamic interactions between non-equilibrium flows and structural components across a wide range of flow regimes. The open-source codes to reproduce the numerical results are available under the MIT license ¹.

Keywords: computational fluid dynamics, kinetic theory, gas kinetic scheme, immersed boundary method, gas-surface interaction

¹<https://github.com/CFDML/TBDVM-Paper>

*Corresponding author

Table 1: Nomenclature.

Symbol	Description
IBM	immersed boundary method
DVM	discrete velocity method
t	time variable
x	space variable
ξ	velocity variable (with its magnitude denoted as ξ)
c	peculiar velocity (with its magnitude denoted as c)
f	particle distribution function
\mathcal{Q}	collision operator of kinetic equation
g	Maxwellian distribution function
g^S	Shakhov equilibrium distribution function
τ	relaxation time
μ	dynamic viscosity
p	pressure
k	Boltzmann constant
ρ	density
n	number density
\mathbf{U}	macroscopic velocity
T	temperature
E	energy
ψ	collision invariants
\mathbf{W}	macroscopic conservative variables $(\rho, \rho\mathbf{U}, \rho E)$
\mathbf{q}	heat flux
N_V	number of collocation points
ω	quadrature weight
ϕ	arbitrary integrable function of ξ
Ω	computational domain
V	volume of domain
\mathbf{F}^f	numerical flux for distribution function
S	area of cell face
\mathbf{n}	outward normal vector of surface
Θ	Heaviside step function
σ	spatial slope of distribution function
f_w^*	surface distribution function considering wall effects
f_w^i	incident particle distribution
f_w^r	reflected particle distribution
α	accommodation coefficient
g_w	surface Maxwellian distribution
ρ_w	density in g_w
\mathbf{U}_w	preconfigured wall velocity

Continued on next page

Symbol	Description
T_w	preconfigured wall temperature
ξ_n	projected particle velocity normal to the boundary
gc, dc, ac	ghost cell, donor cell, auxiliary cell
N_S	number of surface cells
c.c.	cut cell
\mathcal{C}	set of the cut cells' indices
\mathcal{G}	subset of \mathcal{C} with $\xi_n \leq 0$
\mathcal{S}	subset of \mathcal{C} with $\xi_n > 0$
λ	particle mean free path
R_w	boundary curvature radius
θ	proportion of particle velocity exhibiting discontinuity
$[f]$	jump of distribution function
E^*	quadrature error
h, b	reduced distribution functions
H, B	reduced Maxwellian distributions
H^S, B^S	reduced equilibrium distributions
L	characteristic length
γ	specific heat ratio
C	dimensionless sound speed
C_p	pressure coefficient

1. Introduction

Gaseous flows demonstrate distinct behavioral patterns across different regimes. The Knudsen number, defined as the ratio of molecular mean free path to a characteristic length scale, serves as a fundamental parameter for distinguishing flow regimes based on the degree of dilution. Continuum mechanics, e.g., the Euler and Navier-Stokes equations, is rigorously applicable solely under the condition that the Knudsen number is asymptotically small. With the advancement of modern industries (e.g., aerospace technology and advanced chip packaging) towards extreme conditions, rarefied gas dynamics has become increasingly critical, with applications ranging from very-low-earth-orbit flight (when the mean free path is considerably large) [1] to micro-electromechanical system (when the scale of interest becomes small) [2]. Various numerical methods, e.g., stochastic particle methods [3] and deterministic solvers for the Boltzmann equation [4], have been developed to simulate the evolution of rarefied gases.

While numerical methods employing body-conformal meshes remain predominant in flow simulations, the Cartesian grid methodology has been attracting growing attention. In this approach, the computational domain is discretized uniformly using structured grids aligned with Cartesian coordinates. By avoiding cumbersome (re)meshing for specific geometries, the simulation pipeline can be significantly simplified and automated. The regular, structured grids allow straightforward indexing, thus directly supporting higher-order stencil computations [5], optimized memory access, and load balancing. The method is naturally compatible with convergence acceleration techniques, e.g., the multi-grid method [6] and adaptive mesh refinement [7]. Among others, accurate computational modeling of the interaction between gases and immersed objects is a prerequisite for the faithful prediction of flow dynamics and aerodynamic parameters by Cartesian grid methods.

Several approaches have been proposed to model the fluid-structure interaction using the Cartesian grid method. The cut-cell method embeds a curved boundary into the Cartesian mesh by trimming the cell that intersects the geometry into an irregular fluid cell, and computing its reduced volume, partial face areas, and centroids [8]. The governing equations are then applied in these new cells, and the boundary conditions can be directly enforced on the newly created cut edges. The technique is non-intrusive to the solution algorithm and thus easier to implement. It has been applied to particle methods (represented by the direct simulation Monte Carlo) [9–11] and discrete velocity methods of the Boltzmann equation [12] in rarefied gas dynamics. The main challenges of the cut-cell method arise from the tiny, irregular cells created at the boundary. They enforce a severely restrictive time step (often requiring intricate cell-merging [13] or flux-redistribution [14] stabilization), demand elaborate pre-processing (calculating geometric parameters for newly created cells), and break the uniform Cartesian stencils near the wall (resulting in lower-order or one-sided interpolations).

The immersed boundary method (IBM) provides an alternative model for solving fluid-structure coupling. It employs a fixed Cartesian mesh throughout the solution process, thereby avoiding the additional computational complexity caused by the grid cutting. Technically, this approach can be broadly divided into two categories. The first category incor-

porates the notion of introducing a continuous force term within the governing equations to emulate the influence of boundary effects. Since Peskin's original method [15], a series of such methods have been proposed to solve continuum flows, typically represented by (but not limited to) the direct-forcing method [16–18] and penalization method [19–21]. This type of method is also known as the diffused interface method, as the immersed interface can be smeared across multiple meshes due to the use of the discrete delta function or mask function. The second category of methods turns to implicitly model boundary effects by modifying discretization stencils in the solution algorithm, thus eliminating this generally undesirable feature. Representative efforts include the immersed interface method [22, 23] and the ghost-cell-based method [24–29].

A significant challenge inherent to Cartesian grid-based IBM lies in the fact that the number of grids increases at a substantially faster rate with rising Reynolds numbers, compared to a structured body-conformal mesh. This results in prohibitively high computational overheads when applying it to solve extremely high-Reynolds, boundary-layer-dominated flows. In rarefied gas dynamics, the Reynolds number typically remains moderate, and the flow structure is relatively easier to resolve, making it particularly well-suited to leveraging the IBM for addressing multi-body or moving-geometry problems [30]. However, research on IBM for rarefied flows remains notably scarce. Despite considerable efforts to advance the integration of the IBM with the lattice Boltzmann method (LBM, as a simplified discrete velocity model of the Boltzmann equation) and its extended models [31–37], these studies focus primarily on the implementation of no-slip boundary conditions in the continuum limit, thereby failing to predict the phenomena of velocity slip and temperature jump in rarefied flows.

In studies of the IBM for rarefied gaseous flows, Xu et al. improved the suspending grid method and developed an immersed boundary-LBM method that accommodates slip boundaries [38]. Wang et al. integrated the slip model through the penalty feedback immersed boundary technique, thereby expanding the applicability of the Navier-Stokes equations in the slip flow regime [39]. These two methods can effectively predict moderately non-equilibrium flows with Knudsen numbers that are not excessively large. For highly rarefied flows, Pekardan et al. presented three IBM implementations for the discrete velocity method (DVM) of the Boltzmann equation [40]. This work was a pioneering exploration, and its performance has been tested only on right-angle boundaries (and not on curvilinear geometries). Ragta et al. developed a ghost-cell-based IBM for the unified gas-kinetic scheme (as an asymptotic-preserving DVM) [41]. This method employs a relatively large flow-field interpolation stencil, potentially incurring substantial computational overhead and presenting challenges when handling complex three-dimensional geometries. Meanwhile, it utilizes the wall Maxwellian distribution as a supplemental condition for least-squares-based interpolation, which may impair its accuracy in solving strongly non-equilibrium flows. A comprehensive numerical analysis evaluating both the solution accuracy and computational efficiency remains absent.

To address the limitations of current methodologies in accurately capturing non-equilibrium fluid-structure interactions, this study presents an innovative ghost-cell immersed boundary method (GCIBM) for the discrete velocity model of the Boltzmann equation. By adjusting

flow variables in ghost cells, it implicitly incorporates the Maxwell gas-surface interaction model, which enables automatic adaptation of slip velocities and temperature jumps in response to local flow conditions. A particle-velocity-based upwind compact interpolation stencil is proposed to determine wall quantities in the gas-surface interaction model, from which the ghost-cell values are determined. For the space-velocity coupling problem in the Boltzmann equation, a velocity-space cut-cell method is developed to model the discontinuous particle distribution function at the boundary. The proposed interpolation scheme stays well-conditioned for arbitrary geometries. The developed methodology demonstrates universal applicability across all flow regimes for fluid-structure interactions. Comprehensive numerical experiments are performed to validate the proposed method.

The rest of this paper is organized as follows. Section 2 concisely overviews the kinetic theory of gases and the computational framework associated with the discrete velocity method for the Boltzmann model equation. Section 3 provides a detailed description of the ghost-cell immersed boundary method, along with a corresponding numerical analysis of the proposed method. Section 4 includes numerical examples to demonstrate the performance of the current method. The last section presents concluding remarks. The nomenclature is presented in Table 1.

2. Discrete Velocity Method

2.1. Kinetic theory

The discrete velocity method (DVM) is dedicated to numerically solving the Boltzmann equation. In the absence of an external force, the Boltzmann equation for monatomic gases writes

$$\frac{\partial f}{\partial t} + \boldsymbol{\xi} \cdot \nabla_{\mathbf{x}} f = \mathcal{Q}(f), \quad (1)$$

where $f(t, \mathbf{x}, \boldsymbol{\xi})$ denotes the particle distribution function with respect to time $t \in \Gamma \subseteq \mathbb{R}^+$, space $\mathbf{x} \in \mathcal{D} \subseteq \mathbb{R}^D$ and molecular velocity $\boldsymbol{\xi} \in \mathbb{R}^D$, with D the dimension of the problem. The collision term \mathcal{Q} models binary molecular interactions with a five-fold integral operator. Simplified model equations have been developed to reduce the computational complexity for solving the Boltzmann equation. In the Bhatnagar-Gross-Krook (BGK) model [42], the collision integral is replaced by a relaxation operator, i.e.,

$$\mathcal{Q} = \frac{g - f}{\tau}, \quad (2)$$

where g refers to the Maxwellian distribution, i.e.,

$$g = \frac{\rho}{(2\pi RT)^{3/2}} \exp\left(-\frac{c^2}{2RT}\right). \quad (3)$$

Here $\mathbf{c} = \boldsymbol{\xi} - \mathbf{U}$ is the peculiar velocity, c denotes its magnitude, \mathbf{U} is the macroscopic bulk velocity, R is the specific gas constant, and $\{\rho, T\}$ denotes the macroscopic density and temperature, respectively. The relaxation time is defined as $\tau = \mu/p$, where μ and p are the dynamic viscosity and the pressure.

The BGK model establishes the fundamental framework for developing relaxation-type simplifications of the Boltzmann equation. The inherent limitations of the model can be mitigated through the construction of extended models based on it. As an example, to overcome the constraint of a fixed unit Prandtl number in the BGK model, the Shakhov model introduces higher-order correction terms into the equilibrium distribution function, i.e.,

$$g^S = g + g^+ = g \left[1 + (1 - \text{Pr}) \frac{\mathbf{c} \cdot \mathbf{q}}{5pRT} \left(\frac{c^2}{RT} - 5 \right) \right], \quad (4)$$

where Pr is the Prandtl number and \mathbf{q} is the heat flux.

A particle distribution function is related to a unique macroscopic state. The macroscopic conservative variables can be determined by taking moments of the distribution function over velocity space, i.e.,

$$\mathbf{W} = \begin{pmatrix} \rho \\ \rho \mathbf{U} \\ \rho E \end{pmatrix} = \int_{\mathbb{R}^D} f \psi d\boldsymbol{\xi}, \quad (5)$$

where $\psi = (1, \boldsymbol{\xi}, \xi^2/2)^T$ is a vector of collision invariants. The temperature is defined as

$$\frac{D}{2} kT = \frac{1}{2n} \int_{\mathbb{R}^D} c^2 f d\boldsymbol{\xi}, \quad (6)$$

where k is the Boltzmann constant, n is the number density. The pressure and heat flux can be obtained via

$$p = \frac{1}{D} \int_{\mathbb{R}^D} c^2 f d\boldsymbol{\xi}, \quad \mathbf{q} = \frac{1}{2} \int_{\mathbb{R}^D} \mathbf{c} c^2 f d\boldsymbol{\xi}. \quad (7)$$

2.2. Solution algorithm

The Shakhov model is employed to concisely elucidate the core principles of the DVM. With a series of collocation points in a truncated velocity space, the discrete governing equation can be written as

$$\frac{\partial f_k}{\partial t} + \boldsymbol{\xi}_k \cdot \nabla_{\mathbf{x}} f_k = \frac{g_k^S - f_k}{\tau}, \quad k = 1, 2, \dots, N_V, \quad (8)$$

where the subscript k represents the index of the collocation point in the discrete velocity space, N_V is the total number of collocation points, and g_k^S denotes the modified equilibrium distribution function at the k^{th} velocity point. The integral over velocity space can be approximated using numerical quadrature, i.e.,

$$\int_{\mathbb{R}^D} \phi(\boldsymbol{\xi}) d\boldsymbol{\xi} \approx \sum_{k=1}^{N_V} \omega_k \phi_k, \quad (9)$$

where ω_k is the quadrature weight of the k^{th} velocity point, and ϕ represents an arbitrary integrable function with respect to $\boldsymbol{\xi}$, such as that presented from Equation (5) to Equation (7).

Different quadrature rules can be adopted, e.g., the Newton-Cotes and Gauss-Hermite formulas [43].

Equation (8) requires further discretizations in space and time. We first employ the finite volume method for spatial discretization. The cell-averaged distribution function in the control volume Ω_j is defined as

$$f_{j,k} = \frac{1}{V_j} \int_{\Omega_j} f_k dV, \quad (10)$$

where V_j denotes the volume of Ω_j . Integrating Equation (8) over each control volume yields

$$\frac{\partial f_{j,k}}{\partial t} = -\frac{1}{V_j} \int_{\partial\Omega_j} \mathbf{n} \cdot \boldsymbol{\xi}_k f_{\partial\Omega_j,k} dS + \frac{g_{j,k}^S - f_{j,k}}{\tau_j}, \quad (11)$$

where \mathbf{n} is the outward normal vector of the surface of the control volume. The integrand in the above equation can be written as a numerical flux function, i.e.,

$$\mathbf{F}_{\partial\Omega_j,k}^f = \boldsymbol{\xi}_k f_{\partial\Omega_j,k}. \quad (12)$$

Equation (11) can be solved using a time discretization method, e.g., the explicit Euler and multi-stage Runge-Kutta methods [44].

The core task of a finite volume method is the computation of numerical fluxes. Taking the face located at $\mathbf{x}_{j+1/2}$, i.e., the one shared by j -th and $(j+1)$ -th cells, as an example, the distribution function can be constructed based on particle velocity information,

$$f_{j+\frac{1}{2},k} = \Theta(\xi_{n,k}) \left[f_{j,k} + \left(\mathbf{x}_{j+\frac{1}{2}} - \mathbf{x}_j \right) \cdot \boldsymbol{\sigma}_{j,k} \right] + [1 - \Theta(\xi_{n,k})] \left[f_{j+1,k} - \left(\mathbf{x}_{j+1} - \mathbf{x}_{j+\frac{1}{2}} \right) \cdot \boldsymbol{\sigma}_{j+1,k} \right], \quad (13)$$

where Θ is the Heaviside step function and $\xi_{n,k} = \boldsymbol{\xi}_k \cdot \mathbf{n}_{j+1/2}$. The spatial slopes $\{\boldsymbol{\sigma}_j, \boldsymbol{\sigma}_{j+1}\}$ can be obtained using different interpolation stencils with limiters. As an example, a second-order interpolation with the van Leer limiter results in

$$\begin{aligned} \sigma_{j,k}^n &= (\text{sign}(s_1) + \text{sign}(s_2)) \frac{|s_1||s_2|}{|s_1| + |s_2|}, \\ s_1 &= \frac{(f_{j,k}^n - f_{j-1,k}^n)}{(x_j - x_{j-1})}, \quad s_2 = \frac{(f_{j+1,k}^n - f_{j,k}^n)}{(x_{j+1} - x_j)}. \end{aligned} \quad (14)$$

Taking the x -axis direction as an example here, the slopes along other directions can be calculated sequentially. After the distribution function at the face is constructed, the numerical flux can thus be determined,

$$\mathbf{F}_{j+1/2,k}^f = \boldsymbol{\xi}_k f_{j+1/2,k}. \quad (15)$$

2.3. Gas-surface interaction

When solving the Boltzmann equation in the presence of boundaries, the particle distribution function at the wall can generally be formulated based on the particle velocity direction relative to the surface, i.e.,

$$f_{w,k}^* = \begin{cases} f_{w,k}^i, & \boldsymbol{\xi}_k \cdot \mathbf{n}_w \leq 0, \\ f_{w,k}^r, & \boldsymbol{\xi}_k \cdot \mathbf{n}_w > 0, \end{cases} \quad (16)$$

where f_w^* denotes the distribution function at the surface considering wall effects, f_w^i and f_w^r represent incident and reflected particle distributions, respectively, and \mathbf{n}_w is the outward normal vector of the boundary.

The Maxwell model is the most widely adopted gas-surface interaction model to characterize the distribution of reflected particles. In this model, gas molecules are postulated to undergo both diffuse and specular reflections when interacting with solid boundaries. By introducing the accommodation coefficient α , which takes the values 1 and 0 for complete thermal accommodation and perfect momentum conservation limits, respectively, the reflected distribution function can be modeled as

$$f_{w,k}^r = \alpha g_{w,k} + (1 - \alpha) f_{w,k}^s, \quad \boldsymbol{\xi}_k \cdot \mathbf{n}_w > 0. \quad (17)$$

The contribution of diffuse reflections is modeled as a Maxwellian distribution at the wall, i.e.,

$$g_{w,k} = \frac{\rho_w}{(2\pi R T_w)^{3/2}} e^{-\frac{1}{2 R T_w} (\boldsymbol{\xi}_k - \mathbf{U}_w)^2}, \quad (18)$$

where \mathbf{U}_w and T_w are the preconfigured macroscopic velocity and temperature of the solid wall. The contribution of specular reflection can be obtained through

$$f_{w,k}^s = f^s(\mathbf{x}_w, \boldsymbol{\xi}_k, t) = f(\mathbf{x}_w, \boldsymbol{\xi}'_k, t), \quad (19)$$

where $f(\mathbf{x}_w, \boldsymbol{\xi}'_k, t)$ denotes the distribution function of the incoming flow and $\boldsymbol{\xi}'_k$ represents the particle velocity symmetrically mirrored about the tangential plane of the surface with respect to $\boldsymbol{\xi}_k$, which takes the form

$$\boldsymbol{\xi}'_k = \boldsymbol{\xi}_k - 2(\boldsymbol{\xi} \cdot \mathbf{n}_w) \mathbf{n}_w. \quad (20)$$

In this study, we restrict ourselves to cases with fully diffuse boundary conditions, i.e., $\alpha = 1$. To apply Equation (17), the density can be determined using the no penetration condition, i.e.,

$$\int_{\xi_n < 0} \xi_n g_{w,k} d\boldsymbol{\xi} + \int_{\xi_n > 0} \xi_n f_{w,k}^i d\boldsymbol{\xi} = 0, \quad (21)$$

for which the discrete form can be written as

$$\sum_{\xi_{n,k} < 0} \omega_k \xi_{n,k} g_{w,k} + \sum_{\xi_{n,k} > 0} \omega_k \xi_{n,k} f_{w,k}^i = 0, \quad (22)$$

where $f_{w,k}(t)$ denotes the distribution function of the gas at the boundary, and $\xi_{n,k} = \boldsymbol{\xi}_k \cdot \mathbf{n}_w$ is the projected particle velocity normal to the boundary.

3. Immersed Boundary Method

3.1. Problem statement

The gas-surface interaction model in Equation (16) implies a nonlinear Dirichlet problem, where the boundary data depend nonlinearly on the solution of the distribution function. Thus, the numerical implementation of $f_{w,k}$ and potential error origins comprise two principal components:

1. The construction of the distribution of incident particles at the surface ($\xi_k \cdot \mathbf{n}_w < 0$) requires extrapolation of the interior solution;
2. The determination of the distribution of reflected particles at the surface ($\xi_k \cdot \mathbf{n}_w > 0$) involves multiple numerical quadratures.

The numerical errors inherent in formulating the implicit Dirichlet boundary condition are dominated by the lowest-order terms processed in the two components.

A noteworthy characteristic of the kinetic gas-surface interaction model in Equation (16) is the discontinuity near the wall surface. Taking the Maxwell model in Equation (17) as an illustrative case, this discontinuity clearly arises from the disparity between incident and reflected particle distributions, and persists in both physical domain and particle velocity space. Theoretical analysis and numerical investigations have been performed for surfaces of different shapes [45, 46]. The existence of the discontinuity necessitates judicious selection of interpolation schemes and weighting parameters within the boundary formulations to achieve a balance between accuracy, robustness, and flexibility.

The immersed boundary method (IBM) devised in this study furnishes meticulous, point-specific resolutions to the aforementioned challenges. First, the main framework of the IBM method will be introduced in Section 3.2.1. The construction of the distribution function values in the ghost cells meticulously incorporates the effects of surface discontinuities. The methodologies of upwind-weighted interpolation within physical space for the incident particle distribution, alongside the cut-cell correction in velocity space for the reflected particle distribution, will be elucidated in Section 3.2.2 and Section 3.2.3, correspondingly. The numerical analysis of the developed IBM, encompassing interpolation inaccuracies, integration discrepancies, and numerical stability, will be addressed in Section 3.3.

3.2. Solution algorithm

3.2.1. Main framework

The core task of the ghost-cell immersed boundary method (GCIBM) is to integrate the gas-surface interaction model specified by Equation (16) into the solution algorithm through appropriate assignment of ghost-cell values. Note that GCIBMs designed for continuum flows typically arrange image points along the normal direction of the boundary curve to interpolate ghost-cell values [47, 48]. Since the Maxwell gas-surface interaction model in Equation (17) does not explicitly incorporate normal derivatives, we propose a new approach for evaluating ghost-cell values. This technique performs interpolation and construction directly along the Cartesian coordinate axes, circumventing the need for normal projections.

It streamlines the numerical implementation and facilitates extension to three-dimensional and complex geometric topologies.

The computational module for achieving this objective is illustrated in Figure 1. The computational mesh near the gas-solid surface is divided into five types of cells, which can be classified into

1. **Ghost cell:** A cell whose center lies inside the solid region but has at least one neighboring cell, through a shared face, whose center lies in the gas region;
2. **Fluid cell:** A cell whose center lies in the gas region;
3. **Surface cell:** A fluid cell that directly neighbors a ghost cell, either through a face or a corner;
4. **Donor cell:** A surface cell used directly to construct the values in the ghost cell;
5. **Auxiliary cell:** A fluid cell for assisting in the evaluation of spatial gradients in the donor cell;

and two types of points, i.e.,

1. **Intersect point:** A point where the line connecting the center of the ghost cell to the center of its donor cell intersects the solid boundary;
2. **Shifted point:** A point located along the extension of the line from the ghost cell center through the intersect point, positioned at a specified distance beyond the intersection.

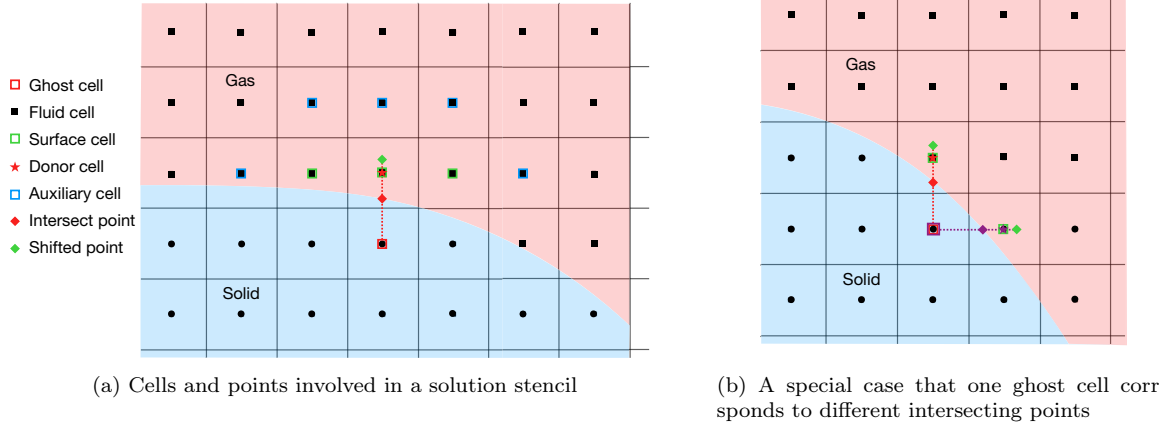


Figure 1: Schematic of the computational module near the gas-solid surface.

Using Figure 1a as an example, we describe the solution algorithm along the y -axis. The same construction approach applies along the rest axes. The method is equally applicable to both two-dimensional and three-dimensional configurations without requiring any dimension-specific adjustments.

1. Shifted point interpolation

It can be demonstrated that if the intersection point potentially overlaps with the center of the donor cell, i.e., the distance between these two points is extremely small, the numerical

error resulting from spatial interpolation based on the donor cell center will be amplified (see Section 3.3.2 for detailed numerical analysis). Therefore, in each donor cell, a shifted point is defined along the line connecting the centers of the ghost and the donor cells. In this study, the position of the shifted point is defined as

$$y_{\text{sp}} = y_{\text{w}} + (y_{\text{dc}} - y_{\text{gc}})/2, \quad (23)$$

where y_{dc} and y_{gc} denote the center positions of the donor and ghost cells, and y_{w} is the location of the intersect point.

The particle distribution function at the shifted point can be approximated using a linear interpolation within the donor cell, i.e.,

$$f_{\text{sp},k} = f_{\text{dc},k} + \sigma_{\text{dc},k}^y (y_{\text{sp}} - y_{\text{dc}}). \quad (24)$$

The spatial slope can be determined as

$$\sigma_{\text{dc},k}^y = \frac{f_{\text{ac},k} - f_{\text{dc},k}}{y_{\text{ac}} - y_{\text{dc}}}, \quad (25)$$

where f_{ac} is the distribution function in the auxiliary cell that is directly adjacent to the donor cell in the y -direction, and y_{ac} denotes its center location.

2. Ghost cell interpolation

Subsequently, we construct the intermediate distribution function in the ghost cell, utilizing the information from the surface cells in Figure 1a. The interpolation formula writes

$$f_{\text{gc},k} = \sum_{j=1}^{N_S} w_{j,k} (f_{j,k} - \boldsymbol{\sigma}_{j,k} \cdot \mathbf{r}_j). \quad (26)$$

where f_j and $\boldsymbol{\sigma}_j$ denote the distribution function and its spatial gradient in the j -th surface cell, and N_S is the total number of surface cells. Note that no superscript $*$ is added in f_{gc} , indicating that it is an intermediate distribution that does not account for the presence of boundaries. The interpolation weights $w_{j,k}$ are constructed in an upwind manner based on particle velocities. The detailed implementation of this construction will be elaborated in the following Section 3.2.2, and the corresponding numerical analysis will be conducted in Section 3.3.4.

3. Intersect point construction

The two intermediate distribution functions constructed above are then used to interpolate the incident distribution function at the intersect point via

$$f_{\text{w},k}^i = f_{\text{sp},k} + \frac{f_{\text{gc},k} - f_{\text{sp},k}}{y_{\text{gc}} - y_{\text{sp}}} (y_{\text{w}} - y_{\text{sp}}). \quad (27)$$

This interpolation method incorporates the combined influence of a hierarchy of surface cells. In contrast to a naive linear extrapolation (as shown by the dashed line in Figure 1a), this

approach is anticipated to mitigate the zigzag effect at Cartesian grid-represented boundaries and reduce non-physical oscillations in the solution. A numerical verification will be presented later in Figure 17.

The incident distribution function in Equation (27) will be used to determine the gas density at the wall surface ρ_w using Equation (22), and the Maxwellian distribution g_w can be computed with Equation (18). The distribution function at the surface considering wall effects f_w^* can then be constructed following Equation (16). The correction for discontinuities in the distribution function in the velocity space induced by the wall surface will be presented in Section 3.2.3.

4. Ghost cell construction

With all necessary information acquired, the particle distribution function in the ghost cell can be constructed as

$$f_{gc,k}^* = f_{sp,k} + \frac{f_{w,k}^* - f_{sp,k}}{y_w - y_{sp}} (y_{gc} - y_{sp}). \quad (28)$$

The derived distribution function subsequently enables the computation of the donor cell's numerical fluxes, as demonstrated in Section 2.2.

3.2.2. Upwind weighting in physical space

For each discrete velocity ξ_k , the advection operator of Equation (8) is hyperbolic over (t, \mathbf{x}) [49, 50]. Thus, the upwind approach is selected to establish the interpolation weights in Equation (26) based on particle velocities, aiming to achieve enhanced numerical stability. Specifically, the interpolation weights are determined via

$$w_{j,k} = \begin{cases} \max(0, \xi_k \cdot \hat{\mathbf{r}}_j)^2 / \sum_{s=1}^{N_S} \max(0, \xi_k \cdot \hat{\mathbf{r}}_s)^2, & \sum_{s=1}^{N_S} \max(0, \xi_k \cdot \hat{\mathbf{r}}_s)^2 \neq 0, \\ 1/N_S, & \sum_{s=1}^{N_S} \max(0, \xi_k \cdot \hat{\mathbf{r}}_s)^2 = 0. \end{cases} \quad (29)$$

Here, the subscript j denotes the index of a surface cell, and $\hat{\mathbf{r}}_j$ is the unit vector pointing from the center of the ghost cell to j -th fluid cell's center. All the N_S surface cells (highlighted with green quadrilateral markers in Figure 1a) participate in determining the weights. Figure 2 illustrates the extreme scenarios where N_S reaches its maximum ($N_S = 7$ for the two-dimensional case; $N_S = 25$ for the three-dimensional case) and minimum ($N_S = 1$) resulting from varying curvature geometries. Note that Equation (26) indicates that different surface cell numbers and interpolation weight selections should solely influence the numerical stability of the solution algorithm, without altering the second-order accuracy.

The fundamental concept embodied in the first line of Equation (29) is: as the direction of ξ_k becomes increasingly aligned with that of \mathbf{r}_j , the molecules at the wall surface with the velocity ξ_k are more likely to be transported from this direction. I.e., this surface cell becomes the predominant contributor to $f_{gc,k}$. In the second line, the relation $\sum_{j=1}^N \max(0, \hat{\xi}_k \cdot \hat{\mathbf{r}}_j)^2 = 0$ implies that these particles are emitted from the solid material rather than originating from the internal flow field. Therefore, even though a direct averaging is employed here, as demonstrated in the intersect point construction in Section 3.2.1, the values of the distribution function $f_{w,k}^*$ at these collocation points will subsequently be

superseded by the Maxwellian distribution $g_{w,k}$, rendering its direct influence on the final solution negligible.

To demonstrate the effectiveness of the proposed upwind interpolation approach, a comparative study will be conducted in Section 4.2, where Figure 17 serves as empirical validation.

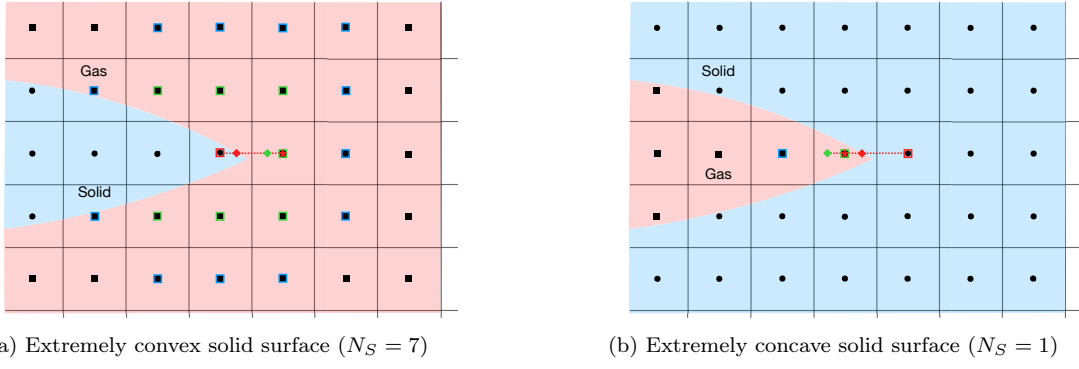


Figure 2: Schematic of the solution stencil when N_S reaches its maximum and minimum.

3.2.3. Cut-cell correction in velocity space

In this work, the composite midpoint rule is employed for numerical quadrature. The quadrature error is generally of second order for a sufficiently continuous integrand in Equation (9). However, discontinuities induced by the wall boundary may potentially result in a reduction in order of accuracy. A detailed mathematical proof will be presented in Section 3.3.3. To address this issue, we develop a cut-cell correction strategy in particle velocity space.

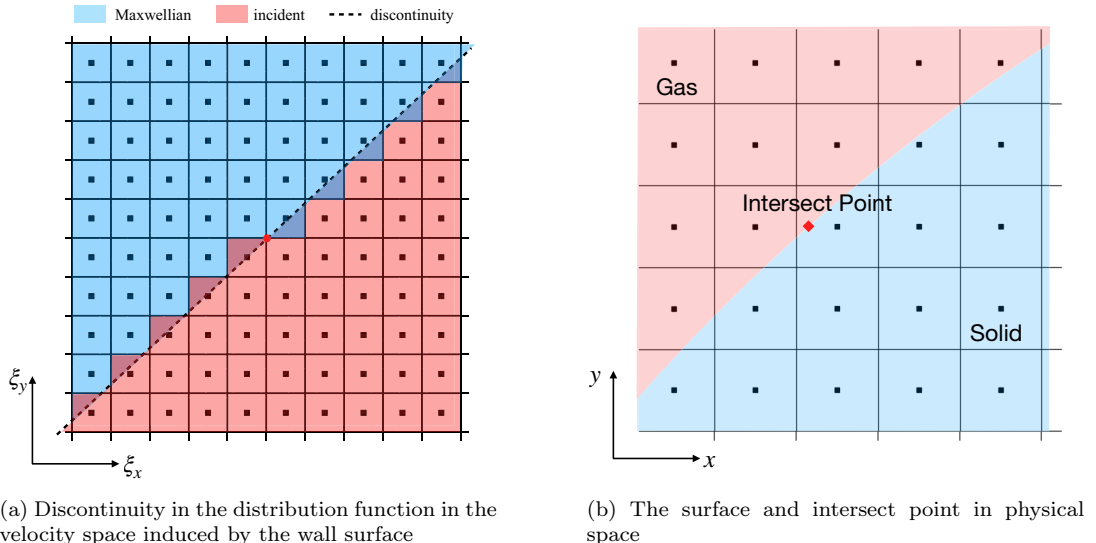


Figure 3: Schematic of the discontinuity in velocity space at the intersect point.

Figure 3a shows an example of the distribution function in the two-dimensional velocity space at the intersection point of the wall surface depicted in Figure 3b. As illustrated, Equation (16) introduces a discontinuity in the distribution function along the tangent to the curved surface (indicated by the dashed line in Figure 3a). As can be seen, the dashed line passes through some velocity cells, which we refer to as cut cells. Ideally, these cells should capture the combined influence of both incident and reflected Maxwellian distributions. However, the piecewise formulation in Equation (16) relying solely on computing $\xi_{n,k} = \boldsymbol{\xi}_k \cdot \mathbf{n}_w$ at the velocity cell center is clearly insufficient for this purpose. As a result, portions of cut cells have been erroneously attributed to the opposite distribution (indicated by semi-transparent shades in Figure 3a).

We employ the following equation to correct the distribution function in a cut cell,

$$\overline{f_{w,k}^*} = \frac{1}{\omega_k} (\omega_k^g f_{w,k}^i + \omega_k^s g_{w,k}), \quad (30)$$

where $\omega_k^g = \Delta \boldsymbol{\xi}_{\text{gas},k}$ and $\omega_k^s = \Delta \boldsymbol{\xi}_{\text{solid},k}$ denote the respective areas occupied by the gaseous and solid phases, as illustrated in Figure 4. The corresponding no penetration condition for

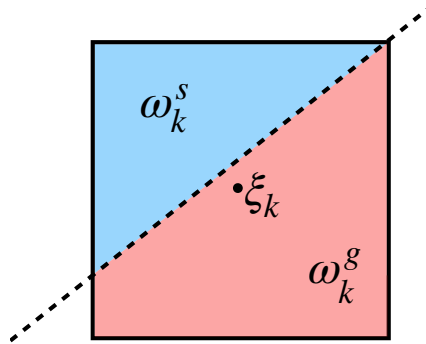


Figure 4: A single cut cell in velocity space.

determining the wall density in Equation (22) becomes

$$\sum_{k \in \text{solid}} \omega_k \xi_{n,k} g_{w,k} + \sum_{k \in \mathcal{C}} \omega_k^s \xi_{n,k} g_{w,k} + \sum_{k \in \text{gas}} \omega_k \xi_{n,k} f_{w,k}^i + \sum_{k \in \mathcal{C}} \omega_k^g \xi_{n,k} f_{w,k}^i = 0, \quad (31)$$

which yields

$$\rho_w = - \frac{\sum_{k \in \text{gas}} \omega_k \xi_{n,k} f_{w,k} + \sum_{k \in \mathcal{C}} \omega_k^g \xi_{n,k} f_{w,k}}{\sum_{k \in \text{solid}} \omega_k \xi_{n,k} G_{w,k} + \sum_{k \in \mathcal{C}} \omega_k^s \xi_{n,k} G_{w,k}}, \quad (32)$$

where $G_{w,k} = \xi_{n,k} \left(\frac{1}{2\pi R T_w} \right)^{3/2} e^{-\frac{1}{2RT_w} (\boldsymbol{\xi}_k - \mathbf{U}_w)^2}$, and c.c. denotes the abbreviation of cut cell. The subscripts *gas* and *solid* in Equation (31) and Equation (32) denote the index sets where the velocity cells fall entirely within the incident and the reflected Maxwellian regions, respectively, and \mathcal{C} is the index sets of cut cells as shown in Figure 3a. Detailed analysis of numerical accuracy of the cut-cell correction will be presented in Section 3.3.3, whereas Section 4.1 provides the numerical verification.

It is known that the terminology “cut cell” typically refers to a sharp-interface fluid-structure interaction model in physical space. We wish to emphasize that the cut-cell correction proposed in this subsection operates in particle velocity space, representing a fundamental difference from the physical-space counterpart. The discontinuity induced by the wall surface exhibits elementary topological structures (straight lines in two-dimensional and planar surfaces in three-dimensional configurations, as shown in Figure 3a). Since Equation (8) does not include a convection operator in velocity space, the small cells that are cut out do not impose strict time-step constraints. These intrinsic properties enable effective optimization of algorithmic complexity and efficient numerical implementation.

3.2.4. Summary

The algorithmic flow of the GCIBM from Section 3.2.1 to Section 3.2.3 is summarized in Figure 5.

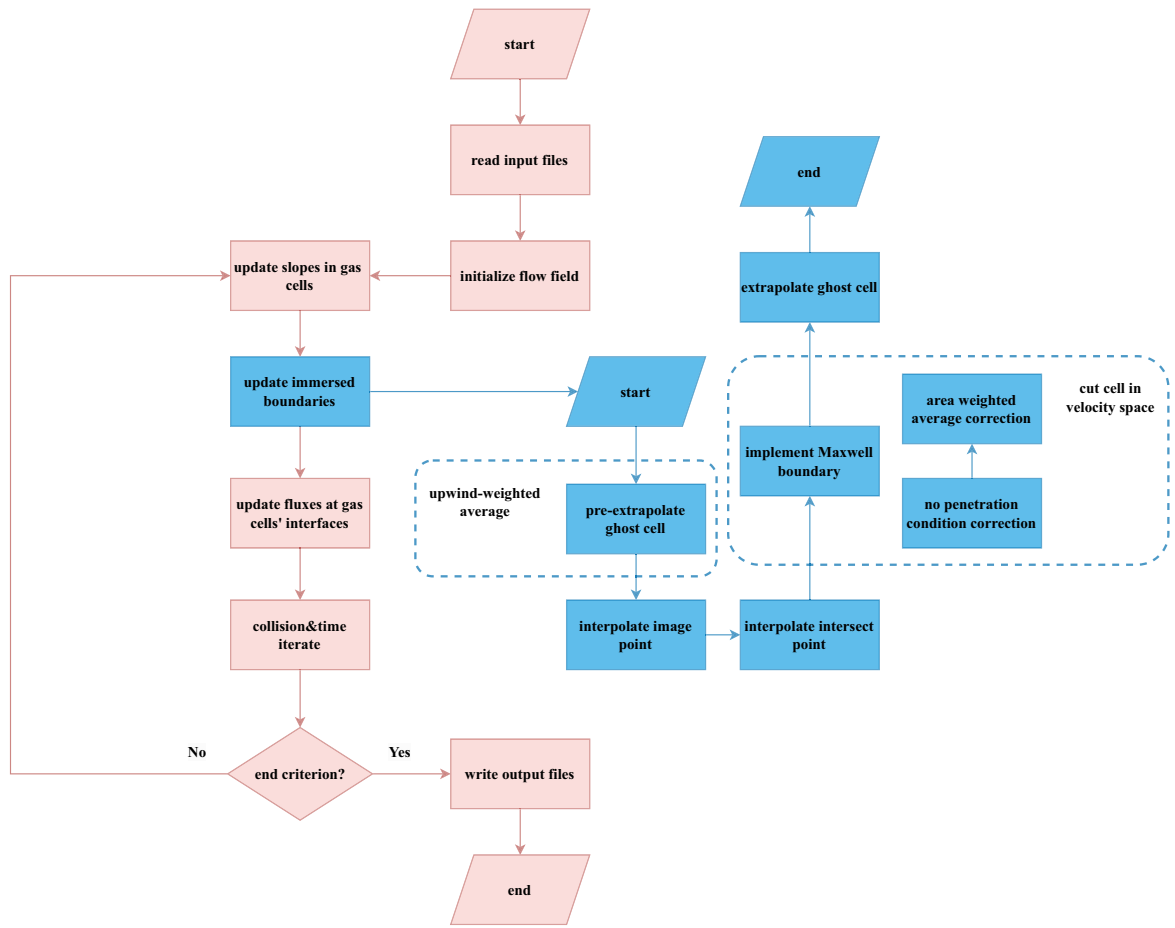


Figure 5: Flow chart of the solution. The boxes labeled with blue refer to the immersed boundary implementation, while those in red represent the outside solution procedure.

3.3. Numerical analysis

3.3.1. Surface discontinuity

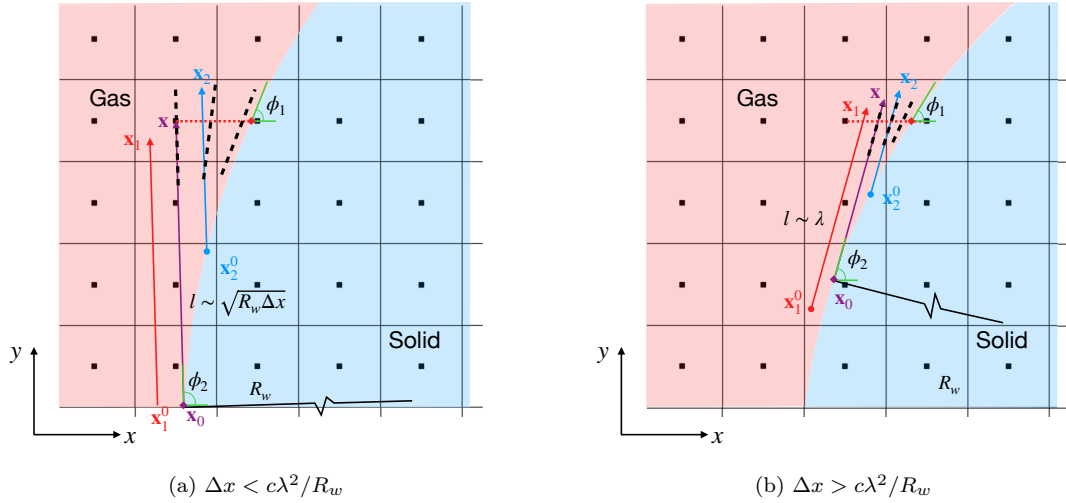


Figure 6: Schematic of the discontinuity induced by convex boundaries. The arrowed lines denote the characteristic lines at the same discrete velocity emitted from different physical points. The red line denotes the characteristic line that is dominated by the gas, the blue denotes the one dominated by the solid boundary, and the purple is tangent to the boundary at \mathbf{x}_0 , along which the discontinuity propagates. The black zigzag line measures the curvature radius of the wall boundary. The black dashed lines denote the approximate location of discontinuities in the distribution function and the direction of discrete velocities. ϕ_1 and ϕ_2 are the angles of tangents at the intersect point (red diamond) of the immersed boundary stencil and the tangency point (purple diamond) between the discontinuous characteristic line and the solid boundary.

Two types of discontinuity phenomena can emerge within gaseous flows. The first type refers to the discontinuity between adjacent gas and predefined wall boundary conditions, caused by the piecewise distribution function in Equation (16). At the macroscopic level, this manifests as the effects of velocity slip and temperature jump. This phenomenon is not directly related to strong discontinuities within the physical space of the gas region. Solvers based on body-conformal meshes as well as the method introduced in Section 3.2.1 should be able to resolve the Knudsen layer without requiring special discontinuity handling strategies. The second type of discontinuity is associated with characteristic lines of the kinetic equation, where the distribution functions at the same velocity position exhibit discontinuities in the physical space. This subsection will specifically address the feasibility of the proposed method under this issue.

The formation of discontinuities in the particle distribution function at the surface of convex objects and their propagation in the physical domain have been confirmed through theoretical analysis [46] and numerical experiments [45]. Figure 6 illustrates the origin of discontinuities from the perspective of characteristic lines. In the two subfigures, the purple line represents the characteristics of the kinetic equation, where the particle velocity falls into the discontinuity region within the velocity space (denoted by the dashed line in Figure 3a).

The characteristic line is tangent to the wall boundary. On either side of a characteristic line, the particle distribution function is determined by the gas (red line) or the solid wall (blue line). Assuming the particle velocity is ξ_k , the characteristic solutions of Equation (8) along the red and blue lines write

$$\begin{aligned} f_k(\mathbf{x}_1, t) &= f_k(\mathbf{x}_1^0, t_1) + \int_{t_1}^t \frac{g_k^S(\mathbf{x}_1 - \xi_k(t' - t_1), t') - f_k(\mathbf{x}_1 - \xi_k(t' - t_1), t')}{\tau(\mathbf{x}_1 - \xi_k(t' - t_1), t')} dt', \\ f_k(\mathbf{x}_2, t) &= g_{w,k}(\mathbf{x}_2^0, t_2) + \int_{t_2}^t \frac{g_k^S(\mathbf{x}_2 - \xi_k(t' - t_2), t') - f_k(\mathbf{x}_2 - \xi_k(t' - t_2), t')}{\tau(\mathbf{x}_2 - \xi_k(t' - t_2), t')} dt', \end{aligned} \quad (33)$$

Here, \mathbf{x}_1 and \mathbf{x}_2 denote points on either side of an arbitrary point \mathbf{x} on the characteristic line, influenced by gas and solid, respectively, while \mathbf{x}_1^0 and \mathbf{x}_2^0 represent their upstream starting points with $t_1 = |\mathbf{x}_1 - \mathbf{x}_1^0|/|\xi_k|$ and $t_2 = |\mathbf{x}_2 - \mathbf{x}_2^0|/|\xi_k|$. Given that $\mathbf{x}_1^0 \rightarrow \mathbf{x}_0$, $\mathbf{x}_2^0 \rightarrow \mathbf{x}_0$ and $t_1 = t_2 = t_*$, we have $\mathbf{x}_1, \mathbf{x}_2 \rightarrow \mathbf{x}$. Note that $f_k(\mathbf{x}_0, t_*)$ and $g_{w,k}(\mathbf{x}_0, t_*)$ can exhibit significant differences. The discontinuity in the physical space thus arises and propagates further along the characteristic line into the gas field. If $\Delta t = t - t_*$ is short enough, the effects of intermolecular collisions can be neglected, and the jump condition of the distribution function at (t, \mathbf{x}, ξ_k) can be written as

$$[f_k(\mathbf{x}, t)] \sim |g_{w,k}(\mathbf{x}_0, t_*) - f_k(\mathbf{x}_0, t_*)|. \quad (34)$$

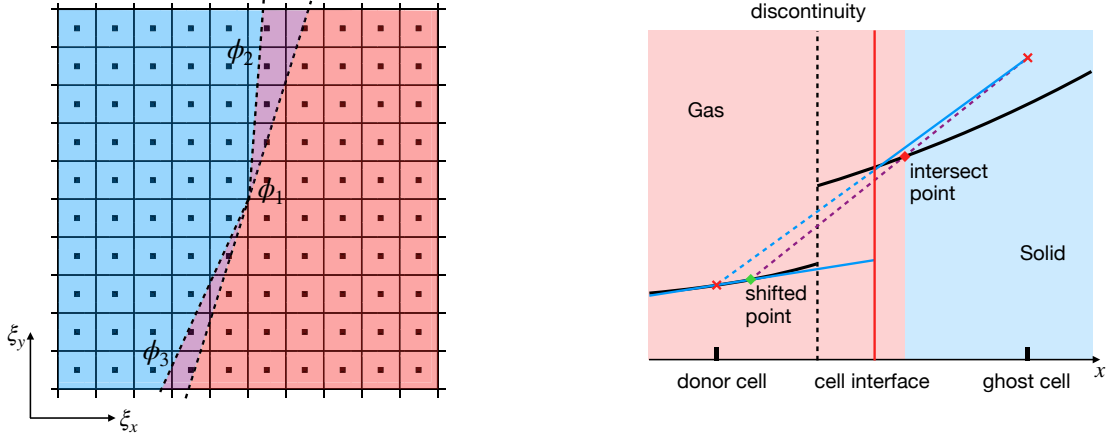
This discontinuity effect decays with intermolecular collisions and is only clearly appreciable within distances on the order of the mean free path [45]. Thus, it appears only at the bottom of the Knudsen layer. Such region containing discontinuities is termed the S layer [51], with a thickness of $O(\lambda \text{Kn}_w)$ magnitude, where λ is the mean free path, and Kn_w denotes the Knudsen number based on the boundary curvature radius R_w , i.e.,

$$\text{Kn}_w = \frac{\lambda}{R_w}. \quad (35)$$

Reviewing the origins of the aforementioned discontinuities, the premise that ξ_k precisely tangents the boundary, coupled with the discontinuity attenuation with collisions, restricts the influence to an exceedingly limited subset of discrete particle velocities. Depending on the relative magnitudes of the mean free path, the curvature radius, the mesh size Δx , and a constant c of $O(1)$ that depends on the geometry of the boundary and the distance between the center of the donor cell and the intersect point, the angle interval of the particle velocity that exhibits discontinuities θ can be estimated as

1. $\Delta x < c\lambda^2/R_w$: $\theta \sim \sqrt{\Delta x/R_w}$. In this case, the mesh resolution is sufficiently high, and thus the discontinuities at different particle velocities can fully occupy the interval between the donor cell and the intersect point, as shown in Figure 6a. Note that discontinuities extending beyond the donor cell belong to internal flow field and can be solved using standard slope limiters; they are not included in the boundary module. Thus, \mathbf{x}_0 is determined by constructing the tangent to boundary passing through the center of the donor cell, and the angle between ϕ_1 and ϕ_2 is determined by Δx and R_w .

2. $\Delta x \geq c\lambda^2/R_w$: $\theta \sim \lambda/R_w$. In this case, the mesh cannot fully resolve the S layer, and discontinuities only exist at the bottom of the interval between the donor cell and intersect point, as shown in Figure 6b. The farthest propagated (with the distance of λ) discontinuity determines the angle between ϕ_1 and ϕ_2 .



(a) Discontinuity proportion in velocity space: the discrete velocities in the purple region exhibit discontinuities within physical space, where ϕ_3 denotes the direction of the tangent from the opposite side

(b) Reconstruction of discontinuous velocities: the black line represents the exact solution, the solid blue line denotes the reconstructed distribution, and the purple line indicates the construction process of the ghost cell

Figure 7: Schematic of the proportion of discontinuous velocities and the approximation of the discontinuity in physical space.

The proportion of discontinuous velocities has been estimated in Figure 7a. For the vast majority of discrete velocity ξ_k , the discrete distribution function f_k remains continuous in physical space. For discontinuous velocities, the approximation process near the boundary is briefly summarized in Figure 7b. The discontinuous solution (black curve) is linearly reconstructed (blue line). With different slopes reconstructed in the donor cell and the ghost cell, the discontinuity effect is modeled at the face. Comparing the blue line and black curve, the error introduced by this process can be estimated as $O([f]\Delta x)$, where $[f] \sim O(1)$ denotes the jump of the discontinuity, and the approximation error is of first order.

Furthermore, in both of the above cases in Figure 6, the characteristic lines of discontinuous velocities graze and point away from the intersect point. This indicates that during the construction of ghost-cell values, these collocation points lie within the region of the reflected velocity space (where the Maxwellian distribution will subsequently be constructed), thus exerting no direct influence on the formulation of wall distribution function. Thus, the design accuracy of $f_{w,k}^i$ and f_w^* should be minimally affected, which further guarantees the validity of the approximation to the distribution in ghost cells.

In engineering simulations, one may be more concerned with macroscopic moments of distribution functions. Considering the application of the quadrature rule, Equation (9), on Equation (5), Equation (6), and Equation (7), the influence of discontinuities is determined by two aspects.

1. The error introduced by discontinuities into the distribution function on each velocity collocation point (estimated as $O(\Delta x)$).
2. The proportion of discontinuous velocities in the velocity space. For an infinite velocity space, this proportion can be estimated as $\theta/2\pi$.

We confine our discussion to boundaries with moderate curvature, i.e., $R_w \sim L$. In the case of $\Delta x \geq c\lambda^2/R_w$ and $\theta \sim \lambda/R_w$, the error induced by the discontinuity to macroscopic variables is thus of $O(\Delta x) \cdot \theta/2\pi$. A suggested height of the first layer mesh is $\Delta x = 0.2\lambda$ [52–54]. Following this requirement, the error can be written as $O(\Delta x) \cdot O(\lambda/R_w) \sim O(\Delta x^2)$, given $\Delta x \sim O(\lambda)$ and $R_w \sim O(1)$. On the other hand, when the mesh are sufficiently refined, i.e., $\Delta x < c\lambda^2/R_w$ and $\theta \sim \sqrt{\Delta x/R_w}$, the error will converge with the order of $O(\Delta x) \cdot O(\sqrt{\Delta x/R_w}) \sim O(\Delta x^{3/2})$.

In summary, the effect of discontinuities at the wall surface is moderate, and the solution algorithm developed in Section 3.2.1 is effective. Note that when the solid boundary contains both convex and concave segments with small characteristic scales of variation, the discontinuity effects can be more complicated, and we do not consider this scenario in the current study.

3.3.2. Spatial accuracy

This subsection proves the developed solution algorithm achieves second-order accuracy for particle velocities that are continuous in the physical space. We firstly introduce a test function of the form

$$f(x, y, \xi) = a(\xi)x + b(\xi)y + c(\xi), \quad (36)$$

where a , b , and c are functions solely of the particle velocity. Without loss of generality, we take the case in Figure 1a as an example. The slope $\sigma(\xi) = [a(\xi), b(\xi)]^T$ applies to all positions in the stencil. Substituting it into Equation (26) and Equation (29) yields

$$f_i(\xi) - \sigma_i(\xi) \cdot r_i = a(\xi)x_{gc} + b(\xi)y_{gc} + c(\xi). \quad (37)$$

Given that the upwind weight $w_i(\xi)$ satisfies $\sum_i^{N_S} w_i(\xi) = 1$, we have

$$f_{gc}(\xi) = [a(\xi)x_{gc} + b(\xi)y_{gc} + c(\xi)] \sum_i^{N_S} w_i(\xi) = a(\xi)x_{gc} + b(\xi)y_{gc} + c(\xi). \quad (38)$$

Similarly, one-sided difference yields $f_{sp}(\xi) = a(\xi)x_{sp} + b(\xi)y_{sp} + c(\xi)$. Substituting it into Equation (27) and noticing that $x_{sp} = x_{gc} = x_w$, we have

$$f_w(\xi) = a(\xi)x_w + b(\xi)y_w + c(\xi), \quad (39)$$

which is in perfect agreement with the exact distribution function at the intersect point. After determining ρ_w with the no penetration condition in Equation (21),

$$\rho_w = -\frac{\int_{\xi_n > 0} \xi_n f_w d\xi}{\int_{\xi_n < 0} \xi_n \left(\frac{1}{2\pi R T_w}\right)^{3/2} e^{-\frac{1}{2 R T_w}((\xi - U_w)^2)} d\xi}, \quad (40)$$

the Maxwell gas-surface interaction in Equation (16) is obtained without spatial discretization error. Subsequently, the accuracy of the boundary condition depends on the extrapolation used to construct $f_{\text{gc}}^*(\boldsymbol{\xi})$.

After Equation (16), the independence of spatial coordinates of a , b , and c is compromised. The analysis based on the test function above no longer holds, and we continue the proof based on the Taylor expansion. Based on the image point, the expansion takes the form

$$f_{\text{w}}^*(\boldsymbol{\xi}) = f_{\text{sp}}(\boldsymbol{\xi}) + \frac{\partial f(x_{\text{dc}}, y, \boldsymbol{\xi})}{\partial y} \bigg|_{y=y_{\text{sp}}} (y_{\text{w}} - y_{\text{sp}}) + O(\Delta y^2), \quad (41)$$

which yields

$$\frac{\partial f(x_{\text{dc}}, y, \boldsymbol{\xi})}{\partial y} \bigg|_{y=y_{\text{sp}}} = \frac{f_{\text{w}}^*(\boldsymbol{\xi}) - f_{\text{sp}}(\boldsymbol{\xi})}{y_{\text{w}} - y_{\text{sp}}} + \frac{O(\Delta y^2)}{y_{\text{w}} - y_{\text{sp}}}. \quad (42)$$

The Taylor expansion also gives

$$f_{\text{gc}}(\boldsymbol{\xi}) = f_{\text{sp}}(\boldsymbol{\xi}) + \frac{\partial f(x_{\text{dc}}, y, \boldsymbol{\xi})}{\partial y} \bigg|_{y=y_{\text{sp}}} (y_{\text{gc}} - y_{\text{sp}}) + O(\Delta y^2). \quad (43)$$

Substituting Equation (42) into the right hand side, we have

$$f_{\text{gc}}(\boldsymbol{\xi}) = f_{\text{sp}}(\boldsymbol{\xi}) + \left(\frac{f_{\text{w}}^*(\boldsymbol{\xi}) - f_{\text{sp}}(\boldsymbol{\xi})}{y_{\text{w}} - y_{\text{sp}}} + \frac{O(\Delta y^2)}{y_{\text{w}} - y_{\text{sp}}} \right) (y_{\text{gc}} - y_{\text{sp}}) + O(\Delta y^2). \quad (44)$$

The order of the truncation error depends on $y_{\text{w}} - y_{\text{sp}}$, i.e., the distance between the image point and the intersect point. When $(y_{\text{gc}} - y_{\text{sp}})/(y_{\text{w}} - y_{\text{sp}}) \sim 1$, the truncation error terms in Equation (44) are consistently of second order. Based on the identification criterion provided in Section 3.2.1, the value of $|y_{\text{w}} - y_{\text{gc}}|$ lies within the interval $(0, \Delta y]$. We suggest the set as Equation (23) for the balance of the accuracy and the physical locality. With the shifted point determined by Equation (23), we obtain

$$f_{\text{gc}}(\boldsymbol{\xi}) = f_{\text{sp}}(\boldsymbol{\xi}) + \frac{f_{\text{w}}^*(\boldsymbol{\xi}) - f_{\text{sp}}(\boldsymbol{\xi})}{y_{\text{w}} - y_{\text{sp}}} (y_{\text{gc}} - y_{\text{sp}}) + O(\Delta y^2), \quad (45)$$

which indicates the reconstruction of ghost-cell values following Equation (28) exhibits a second-order spatial accuracy.

3.3.3. Quadrature accuracy

This subsection demonstrates the effectiveness of the cut-cell correction proposed in Section 3.2.3. As analyzed in Section 3.3.1, at the intersect point, the incident distribution f_{w}^i typically differs from the reflected Maxwellian distribution g_{w} , which forms a discontinuity in the velocity space through Equation (16). We assume $\Delta \xi_x = \Delta \xi_y = \Delta \xi$, and the quadrature weights in Equation (9) takes $\omega_k = \omega = \Delta \xi^2$. We denote the quadrature error by E^* , and the integral over the cut cells writes

$$\int_{\text{c.c.}} \phi f d\boldsymbol{\xi} = \sum_{k \in \mathcal{C}} \omega_k \phi_k f_k + E^* = \omega \left(\sum_{k \in \mathcal{G}} \phi_k f_{\text{w},k}^i + \sum_{k \in \mathcal{S}} \phi_k g_{\text{w},k} \right) + E^*, \quad (46)$$

where \mathcal{C} represents the set of the cut cells' indices, while \mathcal{G} and \mathcal{S} denote the subsets of \mathcal{C} whose elements satisfy $\xi_n = \boldsymbol{\xi}_k \cdot \mathbf{n}_w \leq 0$ and $\xi_n = \boldsymbol{\xi}_k \cdot \mathbf{n}_w > 0$, respectively. Considering the individual continuity of g_w , f_w , and ϕ respectively, the Taylor expansion in the cut cells leads to

$$\begin{aligned}\phi g_w &= \phi_k g_{w,k} + (\boldsymbol{\xi} - \boldsymbol{\xi}_k) \cdot \frac{\partial \phi g_w}{\partial \boldsymbol{\xi}} + O(\Delta \xi^2), \\ \phi f_w^i &= \phi_k f_{w,k}^i + (\boldsymbol{\xi} - \boldsymbol{\xi}_k) \cdot \frac{\partial \phi f_w^i}{\partial \boldsymbol{\xi}} + O(\Delta \xi^2).\end{aligned}\quad (47)$$

Applying Equation (47) to cut cells yields

$$\begin{aligned}\iint_{\mathcal{C}} \phi f d\boldsymbol{\xi} &= \sum_{k \in \mathcal{C}} \left[\iint_{\Delta \boldsymbol{\xi}_{\text{gas},k}} (\phi_k f_{w,k}^i + O(\Delta \xi)) d\boldsymbol{\xi} + \iint_{\Delta \boldsymbol{\xi}_{\text{solid},k}} (\phi_k g_{w,k} + O(\Delta \xi)) d\boldsymbol{\xi} \right] \\ &= \sum_{k \in \mathcal{G}} \left[\iint_{\Delta \boldsymbol{\xi}_k} \phi_k f_{w,k}^i d\boldsymbol{\xi} + \iint_{\Delta \boldsymbol{\xi}_{\text{solid},k}} \phi_k (g_{w,k} - f_{w,k}^i) d\boldsymbol{\xi} + O(\Delta \xi^3) \right] + \\ &\quad \sum_{k \in \mathcal{S}} \left[\iint_{\Delta \boldsymbol{\xi}_k} \phi_k g_{w,k} d\boldsymbol{\xi} + \iint_{\Delta \boldsymbol{\xi}_{\text{gas},k}} \phi_k (f_{w,k}^i - g_{w,k}) d\boldsymbol{\xi} + O(\Delta \xi^3) \right] \\ &= \omega \left(\sum_{k \in \mathcal{G}} \phi_k f_{w,k}^i + \sum_{k \in \mathcal{S}} \phi_k g_{w,k} \right) + \sum_{k \in \mathcal{G}} \iint_{\Delta \boldsymbol{\xi}_{\text{solid},k}} \phi_k (g_{w,k} - f_{w,k}^i) d\boldsymbol{\xi} + \\ &\quad \sum_{k \in \mathcal{S}} \iint_{\Delta \boldsymbol{\xi}_{\text{gas},k}} \phi_k (f_{w,k}^i - g_{w,k}) d\boldsymbol{\xi} + O(\Delta \xi^2)\end{aligned}\quad . \quad (48)$$

Here, $\Delta \boldsymbol{\xi}_{\text{gas},k}$ and $\Delta \boldsymbol{\xi}_{\text{solid},k}$ represent the partition of the two distribution function to the k -th cut cell. The last equality is obtained with the estimation that the number of the cells that the discontinuity goes through is of comparable magnitude to $\sqrt{N_V} \sim \sqrt{RT_0}/\Delta \xi$, where R is the gas constant and T_0 is the reference temperature. Comparing Equation (48) with Equation (46), we obtain

$$E^* = \sum_{k \in \mathcal{G}} \iint_{\Delta \boldsymbol{\xi}_{\text{solid},k}} \phi_k (g_{w,k} - f_{w,k}^i) d\boldsymbol{\xi} + \sum_{k \in \mathcal{S}} \iint_{\Delta \boldsymbol{\xi}_{\text{gas},k}} \phi_k (f_{w,k}^i - g_{w,k}) d\boldsymbol{\xi} + O(\Delta \xi^2). \quad (49)$$

In extreme cases (depending on the normal vector of the boundary), we have $\Delta \boldsymbol{\xi}_{\text{solid},k} \sim \Delta \boldsymbol{\xi}_{\text{gas},k} \sim 0.5 \Delta \boldsymbol{\xi}_k \sim \Delta \xi^2$, and the error can be estimated as

$$E^* \sim \sqrt{N_V} \omega |\overline{\phi(g_w - f_w^i)}| \sim \frac{1}{\Delta \xi} \Delta \xi^2 |\overline{\phi(g_w - f_w^i)}| = \Delta \xi |\overline{\phi(g_w - f_w^i)}| \sim O(\Delta \xi), \quad (50)$$

where $|\overline{\phi(g_w - f_w^i)}|$ represents the average difference between the Maxwellian and extrapolated non-equilibrium distribution over the cut cells. The conclusion depends on the premise that $\Delta \xi \ll |\phi(g_w - f_w^i)|$, i.e., the resolution is fine enough to resolve the variation of $\phi(\boldsymbol{\xi})$.

We wish to point out the above issues also exist for higher-order quadrature. For the closed curve boundary, the discontinuities at different boundary points will sweep over the

whole velocity space, which makes the correction by adopting the specific quadrature points distribution invalid. Employing different collocation points at different locations can be helpful. However, this requires mappings between different collocation points, thereby complicating the computational process and introducing additional aliasing errors. The cut-cell method in velocity space represents a more readily implementable approach. We return to the second equality in Equation (48). If the quadrature on $\Delta\xi_{\text{gas},k}$ and $\Delta\xi_{\text{solid},k}$ is handled separately, we arrive at

$$\begin{aligned}
\iint_{c.c.} \phi f d\xi &= \sum_{k \in \mathcal{C}} \left(\iint_{\Delta\xi_{\text{gas},k}} \phi f_w^i d\xi + \iint_{\Delta\xi_{\text{solid},k}} \phi g_w d\xi \right) \\
&= \sum_{k \in \mathcal{C}} \left[\iint_{\Delta\xi_{\text{gas},k}} (\phi_k f_{w,k}^i + O(\Delta\xi)) d\xi + \iint_{\Delta\xi_{\text{solid},k}} (\phi_k g_{w,k} + O(\Delta\xi)) d\xi \right] \\
&\sim \sum_{k \in \mathcal{C}} (\phi_k (\Delta\xi_{\text{gas},k} f_{w,k}^i + \Delta\xi_{w,k} g_{w,k}) + O(\Delta\xi) \Delta\xi^2) \\
&\sim \sum_{k \in \mathcal{C}} \Delta\xi_k \phi_k \overline{f_{w,k}^*} + \sqrt{N_V} \Delta\xi^2 O(\Delta\xi) \\
&\sim \sum_{k \in \mathcal{C}} \Delta\xi_k \phi_k \overline{f_{w,k}^*} + O(\Delta\xi^2)
\end{aligned}, \quad (51)$$

where

$$\overline{f_{w,k}^*} = \frac{\Delta\xi_{\text{gas},k}}{\Delta\xi_k} f_{w,k}^i + \frac{\Delta\xi_{w,k}}{\Delta\xi_k} g_{w,k} = \frac{1}{\omega_k} (\omega_k^g f_{w,k}^i + \omega_k^s g_{w,k}), \quad (52)$$

which is exactly Equation (30). Hence, the quadrature accuracy has been improved to the the second order. A numerical validation will be presented in Figure 18.

3.3.4. Stability and well-posedness

Finally, we analyze the necessity of the upwind interpolation approach. To elucidate the motivation and effectiveness of the approach, we firstly identify the source of numerical instability in the IBM based on the direction of the characteristic lines of the kinetic equation. Due to the introduction of immersed boundaries, the mesh face may not coincide with the solid boundary. Consequently, the advection operator of the kinetic equation at some discrete velocities (belonging to the incident portion) can be interpreted as being solved with a fully downwind scheme, which is known for its numerical instability.

Referring to Figure 8, we elaborate on the root cause of the issue. In Figure 8b, the red and purple parts constitute the incident distribution function, where the particle velocity satisfies $\xi_{n,k} < 0$. As introduced in Section 3.2.1, the distribution function of the ghost cell is extrapolated along x -direction. Using it to compute the numerical fluxes at the face labeled with red line in Figure 8a, we can obtain the semi-discrete equation for the donor cell $(\mathbf{x}_i, \mathbf{y}_j)$ at ξ_k , i.e.,

$$\frac{\partial f_{i,j,k}}{\partial t} + \frac{\xi_{x,k}}{\Delta x} (f_{i+\frac{1}{2},j,k} - f_{i-\frac{1}{2},j,k}) = \frac{g_{i,j,k}^S - f_{i,j,k}}{\tau_{i,j}} - \frac{\xi_{y,k}}{\Delta y} (f_{i,j+\frac{1}{2},k} - f_{i,j-\frac{1}{2},k}). \quad (53)$$

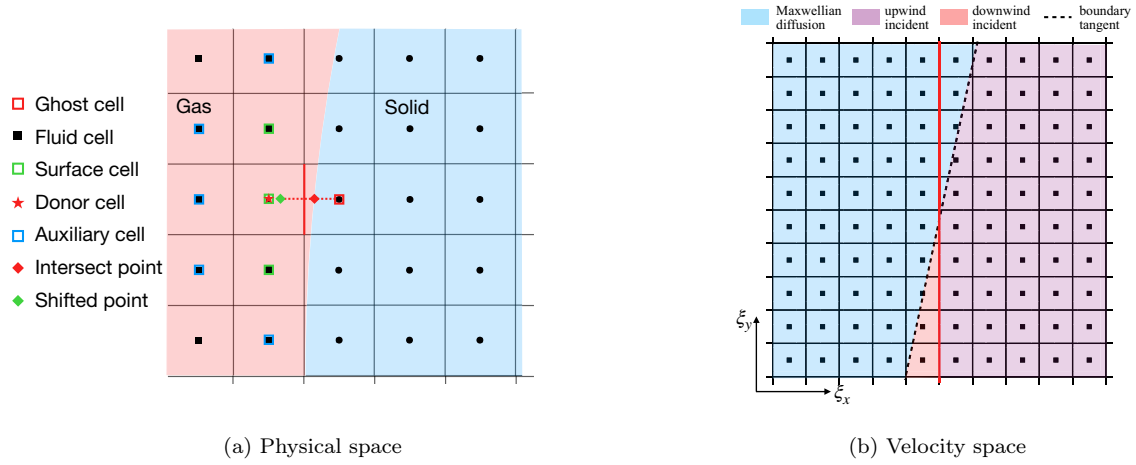


Figure 8: Schematic showing the origin of numerical instability. In this case, the downwind collocation points are of small proportion and the stability can be maintained with sufficient collisions.

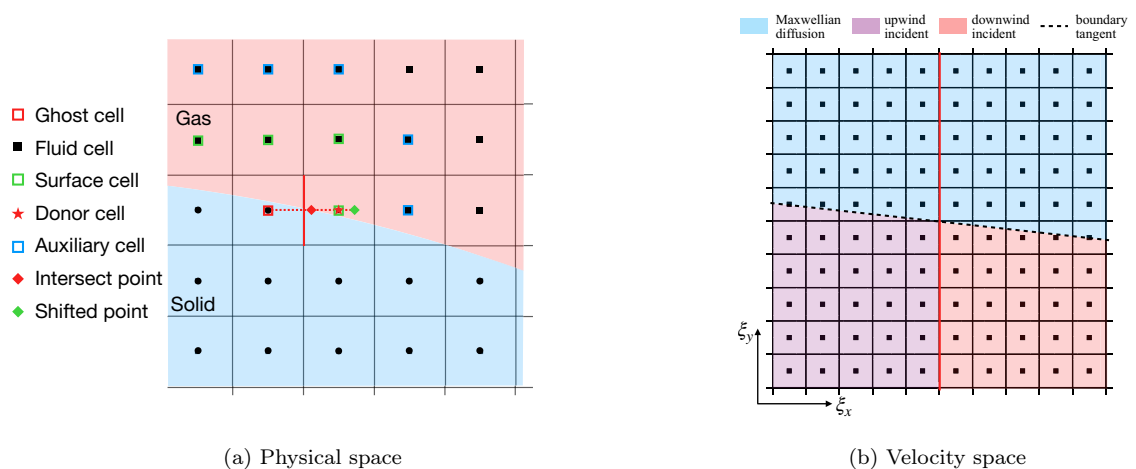


Figure 9: Schematic showing the origin of numerical instability. In this case, the downwind collocation points are of large proportion and the solution tends to be unstable from the donor cell.

Hereafter we omit the collision term and fluxes along y -direction (non-related to the immersed boundary).

The discrete velocities that fall into the incident region satisfy

$$\xi_{n,k} < 0 \quad \text{and} \quad \xi_{x,k} < 0. \quad (54)$$

Without the upwind-weighted strategy, the construction of distribution function in the ghost cell can be written as

$$\begin{aligned} f_{i+1,j,k} &= 2f_{i,j,k} - f_{i-1,j,k}, \\ \sigma_{i+1,j,k}^x &= \frac{1}{\Delta x}(f_{i,j,k} - f_{i-1,j,k}) \end{aligned} \quad (55)$$

Substituting $f_{i\pm\frac{1}{2},j,k}$ provided in Equation (13) into the left-hand side of Equation (53), we arrive at

$$\frac{\partial f_{i,j,k}}{\partial t} + \frac{\xi_{x,k}}{\Delta x}(f_{i,j,k} - f_{i-1,j,k}) = 0. \quad (56)$$

Given that $\xi_{x,k} < 0$, the advection operator is discretized with a downwind scheme along x -direction, which can cause the numerical instability. Note that the existence of downwind collocations is entirely attributed to the non-coincidence of mesh face with solid boundary. If the two are aligned, we have

$$\xi_{n,k} = -\xi_{x,k}, \quad (57)$$

and Equation (54) will not hold.

The above analysis does not account for the effect of collision term. Preliminary studies have been conducted on collision effects in the near-Maxwellian regime [55]. While still in the nascent stages, initial findings suggest that collision terms exert a stabilizing influence upon the numerical system. For the case of Figure 8, the portion of the downwind region is very low. The instability induced by the downwind scheme is expected to be counteracted by collision effects. For the case of Figure 9, the influence exerted by the downwind portion is stronger, making it more difficult for a naive interpolation method to maintain the stability. More systematic work on collision term analysis will be carried out in future endeavors.

We wish to point out that, when viewed through an alternative lens, the solution of the advection operator using a downwind scheme should require an additional inflow boundary condition along x -direction. Due to the finite numerical resolution, direct interpolation without the upwind-weighted strategy can fail to meet this requirement, leading to the ill-posedness in the discretized algebraic system. From the perspective of particle transports, particles with downwind velocities transport tangentially along the wall surface, indicating that additional information should be provided from other dimensions. This inspires us to develop the upwind-weighted strategy.

4. Numerical Experiments

This section validate the solution algorithm through numerical experiments. Both two-dimensional and three-dimensional fluid-structure interactions are considered. For two-

dimensional problems, we employ reduced distribution functions to enhance the computational efficiency [56], which are defined as

$$h = \int_{-\infty}^{\infty} f d\xi_z, \quad b = \int_{-\infty}^{\infty} \xi_z^2 f d\xi_z, \quad (58)$$

where ξ_z represents the molecular velocity along z -direction. The non-dimensionalization is performed as

$$\begin{aligned} \hat{x}_i &= \frac{x_i}{L}, \quad \hat{\rho} = \frac{\rho}{\rho_0}, \quad \hat{T} = \frac{T}{T_0}, \quad \hat{\xi}_i = \frac{\xi_i}{\sqrt{2RT_0}}, \quad \hat{U}_i = \frac{U_i}{\sqrt{2RT_0}}, \quad \hat{\mu} = \frac{\mu}{\rho_0 L \sqrt{2RT_0}}, \\ \hat{p} &= \frac{p}{2\rho_0 RT_0}, \quad \hat{q}_i = \frac{q_i}{\rho_0 (2RT_0)^{3/2}}, \quad \hat{h} = \frac{h}{\rho_0 / (2RT_0)}, \quad \hat{b} = \frac{b}{\rho_0}, \end{aligned} \quad (59)$$

where L represents a macroscopic characteristic length. The subscript 0 denotes the reference state. For brevity, we omit the hat notation henceforth. With above non-dimensionalization, the reduced Maxwellian and corrected equilibrium distributions write

$$\begin{aligned} H_k &= \frac{\rho}{\pi T} e^{-\frac{c_k^2}{T}}, \quad B_k = \frac{T}{2} H_k \\ H_k^S &= H_k \left[1 + \frac{4(1-Pr)}{5\rho T^2} \mathbf{c}_k \cdot \mathbf{q} \left(\frac{2c_k^2}{T} - 4 \right) \right]. \\ B_k^S &= B_k \left[1 + \frac{4(1-Pr)}{5\rho T^2} \mathbf{c}_k \cdot \mathbf{q} \left(\frac{2c_k^2}{T} - 2 \right) \right] \end{aligned} \quad (60)$$

Argon gas is used in all numerical experiments and variable hard sphere (VHS) model is adopted to determine the reference dynamic viscosity,

$$\mu_0 = \frac{5(\alpha+1)(\alpha+2)\sqrt{\pi}}{4\alpha(5-2\omega)(7-2\omega)} \text{Kn}, \quad (61)$$

where $\alpha = 1.0$ and $\omega = 0.81$ for Argon. The local viscosity is determined by

$$\mu = \mu_0 \left(\frac{T}{T_0} \right)^\omega. \quad (62)$$

The convergence criterion is set as

$$\text{res} = \max_i \frac{\sqrt{\sum_j^N (\mathbf{W}_{i,j}^{n+1} - \mathbf{W}_{i,j}^n)^2}}{\sum_j^N |\mathbf{W}_{i,j}^{n+1}|} < \text{TOL}, \quad (63)$$

where $W_{i,j}^n$ represents the i -th macroscopic conservative variable in the j -th physical cell and n -th time step, N denotes the total number of the mesh in physical space. In this paper, we set the tolerance as $\text{TOL} = 10^{-6}$. The forward Euler scheme is adopted for time marching in all cases.

4.1. Convergence test

We first test the convergence of the solution algorithm using a lid-driven cavity flow, and an additional stationary cylinder with diameter $D = 0.25$ is positioned at the center of the cavity. The characteristic length is defined as the cavity length ($L = 1.0$), while the lid velocity is set to $U_w = 0.15$. The temperature of all solid walls are set as $T_w = 1.0$. The Knudsen number in the reference state is 0.075.

We first test the convergence in the velocity space. A series of uniform collocation points with resolutions of 40×40 , 60×60 , 80×80 , and 100×100 are used in the truncated velocity space $[-5, 5]^2$. The converged solution on the velocity mesh of 200×200 is adopted as the reference, which is shown in Figure 10. The Cartesian mesh in the physical space is fixed at 64×64 .

The order of convergence is shown in Figure 12. The L_1 error of the temperature is measured at the wall of the cylinder, i.e., the intersect points in Figure 1a. The solution algorithm with and without the cut-cell method exhibits second- and first-order accurate convergence, respectively, which is consistent with the analysis in Section 3.2.3. Figure 13 shows the comparison of the wall temperature with the same velocity mesh of 40×40 . It is clear that the accuracy is remarkably improved and further validates the effectiveness of the proposed cut-cell methodology in velocity space.

For convergence testing in physical space, since numerical solution obtained with fine mesh remain inevitably susceptible to the zigzag effect, we construct an exact reference solution of the form

$$\begin{aligned} h_k &= \frac{\rho^*}{\pi T^*} e^{-\frac{\xi_k - \mathbf{U}^*}{T^*}}, \quad b_k = \frac{T^*}{2} h_k, \\ \rho^* &= 1 + 0.1 \sin \pi(x + y), \quad T^* = 1 + 0.1 \cos \pi(x + y), \\ \mathbf{U}^* &= 0.4[\sin \pi(x + y), \cos \pi(x + y)]^T. \end{aligned} \quad (64)$$

For the above solution, we can analytically determine the distribution function at the wall of the cylinder, and use it as the benchmark solutions to measure the numerical error introduced by the numerical method in a time step. A series of uniform Cartesian mesh in physical space with the resolution of 64×64 , 128×128 , and 256×256 are employed. The velocity collocation points are fixed at 120×120 . The L_1 and L_∞ errors of the temperature are shown in Figure 11, where the second-order spatial accuracy proved in Section 3.3 is validated.

4.2. Hypersonic flow around circular cylinder

The second numerical experiment is the hypersonic flow around a cylinder. The Mach number is set as 5.0 and the Knudsen number is 0.1. The radius of the cylinder serves as the characteristic length, i.e., the dimensionless radius of the cylinder $R_0 = 1.0$. The state of the incoming flow serves as the reference state, i.e. the dimensionless density $\rho_\infty = 1.0$, and temperature $T_\infty = 1.0$. The dimensionless freestream velocity is calculated with

$$U_\infty = \text{Ma}C_\infty, \quad (65)$$

where the dimensionless sound speed $C_\infty = \sqrt{\gamma T_\infty / 2}$. For Argon gas, the specific heat ratio $\gamma = 5/3$. The temperature of the cylinder wall is $T_w = 1.0$. The physical domain is set as

$[-16, 16]^2$, with a stationary cylinder positioned at $(0, 0)$. As shown in Figure 14, a tree-based adaptive mesh refinement (AMR) strategy is employed to enhance the numerical efficiency, where the mesh size adjacent to the solid boundary is set as 0.01 (configured with reference to the body-fitted mesh [53]). The velocity space is truncated as $[-10, 10] \times [-10, 10]$ and discretized with a uniform Cartesian mesh of 60×60 .

The convergent distributions of density, velocity, temperature, and heat flux are presented in Figure 15. No obvious non-physical oscillations are observed, even in the region immediately adjacent to the cylinder. The comparison of wall quantities with DSMC and a body-conformal DVM [53] is provided in Figure 16. The simulation results exhibit excellent consistency with the reference solution.

The slipping velocities along the wall surface obtained by the current method with and without the upwind weighting strategy in Equation (29) are shown in Figure 17. It can be seen that the results without upwind weighted average exhibit severe numerical oscillations, especially at the top of the cylinder where a longer horizontal mesh trail is used to represent the boundary. Such trail introduces prominent spurious geometric effects. To address this issue, the upwind weighted average utilizes the information from both x and y directions. This can be understood as the reasonable incorporation of artificial viscosity, which substantially improve the numerical stability.

To elucidate the nature of the Maxwell gas-surface interaction model, the distribution function in the velocity space at the wall boundary is shown in Figure 18. The three-dimensional plot in Figure 18b clearly explains the discontinuity in the velocity space, which results in a reduction in order of accuracy and necessitates the cut-cell correction.

4.3. Supersonic flow around NACA0012 airfoil

The next numerical experiment is the flow around a NACA0012 airfoil [57]. The chord length serves as the characteristic length, i.e., the dimensionless chord length $L_c = 1.0$. The Mach number and the Knudsen number are 2.0 and 0.026, respectively. The density, velocity and temperature are respectively nondimensionalized by the incoming flow. The dimensionless temperature of the airfoil surface T_w is fixed at 1.0. The angle of attack is 0. The physical domain and the mesh size used for resolving the boundary flows follows the settings in [58]. The domain is $[-3, 7] \times [-7, 7]$, where the leading edge of the airfoil is positioned at $(0, 0)$. The number of surface meshes in the refined region is around 600. A uniform Cartesian mesh with the resolution of 60×60 in the range of $[-4, 8] \times [-6, 6]$ is employed in the velocity space.

The distribution of density, velocity, temperature, and heat flux are shown in Figure 19. The numerical results show good agreement with those reported in [57]. To quantify the computational accuracy of wall variables, we compare the surface pressure coefficient defined as

$$C_p = \frac{2(p_w - p_0)}{\rho_0 U_0^2}. \quad (66)$$

The reference solutions are computed using a body-conformal DVM solver [59, 60] based on an unstructured mesh and the SPARTA DSMC simulator [61]. The minimum mesh size in the unstructured mesh is identical to that for the Cartesian mesh, and the converged

simulation results are shown in Figure 20, where the minimum mesh size is 0.003. The comparison of wall physical quantities is shown in Figure 21, which confirms the consistency of results obtained through different methods.

4.4. Supersonic flow around a sphere

The last numerical experiment aims to validate the performance of the solution algorithm in three-dimensional problems. In this case, supersonic flow around a sphere with the Mach number $Ma = 3.834$ and Knudsen number $Kn = 0.03$ is simulated. The diameter of the sphere serves as the characteristic length. The reference density and temperature are from the incoming flow. The temperature at the sphere is fixed at $T_w = [1 + (\gamma - 1)Ma^2/2]T_0$, where T_0 is the reference temperature. The physical domain is set as $[-4, 4]^3$, and the minimum interval of the refined mesh is $\Delta x = 0.02$. To further reduce the computational cost, a locally refined Cartesian mesh is employed in the truncated velocity space $[-3\sqrt{T_w}, 3\sqrt{T_w}]^3$, which is shown in Figure 22, and the minimum mesh size is $\Delta\xi = 0.2275$.

The distributions of density, velocity, temperature, and heat flux near the wall surface can be found in Figure 23 and Figure 24. Figure 25 provides a quantitative comparison with the results in [53]. The comparative study demonstrates satisfactory consistency and validates the current method for three-dimensional fluid-structure interactions.

5. Conclusion

Computational modeling and simulation of dynamic interactions between non-equilibrium flows and structural components serve as indispensable tools for advancing aerospace research. In this paper, an immersed boundary method is developed for the discrete velocity model of the Boltzmann equation within the Cartesian grid framework. The proposed approach employs a particle-velocity-based upwind compact interpolation strategy to improve numerical stability for arbitrary immersed boundaries, and incorporates a velocity-space cut-cell correction to ensure quadrature accuracy in the presence of discontinuities of particle distribution function. The method accurately characterizes velocity slip and temperature jump effects and achieves reliable prediction of aerodynamic parameters. Owing to its dimension-independent formulation, the method can be equally applied to two- and three-dimensional problems. Numerical results for a variety of benchmark problems demonstrate that the proposed solution algorithm achieves accuracy comparable to body-conformal solvers while retaining the simplicity, flexibility and scalability of the Cartesian grid method. This investigation confines its scope to fixed rigid boundaries. Extensive study of moving and deformable structures will be considered in future work.

Acknowledgements

The current research is funded by Strategic Priority Research Program of Chinese Academy of Sciences (XDB0620403), Chinese Academy of Sciences Project for Young Scientists in Basic Research (YSBR107), National Science Foundation of China (12302381, 12572340), and Beijing Natural Science Foundation (L252039). The computing resources provided by Hefei Advanced Computing Center are acknowledged.

References

- [1] J Virgili Llop, PC Roberts, Zhou Hao, L Ramio Tomas, and Valentin Beauplet. Very low earth orbit mission concepts for earth observation: Benefits and challenges. In *Reinventing Space Conference*, pages 18–21, 2014.
- [2] Mohamed Gad-el Hak. *MEMS: introduction and fundamentals*. CRC press, 2005.
- [3] G.A. Bird. *The DSMC Method*. CreateSpace Independent Publishing Platform, 2013.
- [4] James E. Broadwell. Study of rarefied shear flow by the discrete velocity method. *Journal of Fluid Mechanics*, 19(3):401–414, July 1964.
- [5] Liu Peng, Richard Seymour, Ken-ichi Nomura, Rajiv K Kalia, Aiichiro Nakano, Priya Vashishta, Alexander Laddoch, Michael Netzband, William R Volz, and Chap C Wong. High-order stencil computations on multicore clusters. In *2009 IEEE International Symposium on Parallel & Distributed Processing*, pages 1–11. IEEE, 2009.
- [6] Ulrich Trottenberg, Cornelius W Oosterlee, and Anton Schuller. *Multigrid methods*. Academic press, 2001.
- [7] Tomasz Plewa, Timur Jaan Linde, and Vincent Gregory Weirs, editors. *Adaptive mesh refinement, theory and applications: proceedings of the Chicago Workshop on Adaptive Mesh Refinement Methods, Sept. 3-5, 2003*. Number 41 in Lecture notes in computational science and engineering. Springer, Berlin ; New York, 2005. Meeting Name: Chicago Workshop on Adaptive Mesh Refinement Methods OCLC: ocm57285503.
- [8] David M Ingram, Derek M Causon, and Clive G Mingham. Developments in cartesian cut cell methods. *Mathematics and Computers in Simulation*, 61(3-6):561–572, 2003.
- [9] Chonglin Zhang and Thomas E Schwartzentruber. Robust cut-cell algorithms for dsmc implementations employing multi-level cartesian grids. *Computers & fluids*, 69:122–135, 2012.
- [10] Wenjie Jin, J Ruud van Ommen, and Chris R Kleijn. A new cut-cell algorithm for dsmc simulations of rarefied gas flows around immersed moving objects. *Computer Physics Communications*, 212:146–151, 2017.
- [11] Steve J Plimpton, SG Moore, A Borner, AK Stagg, TP Koehler, JR Torczynski, and MA Gallis. Direct simulation monte carlo on petaflop supercomputers and beyond. *Physics of Fluids*, 31(8), 2019.
- [12] G. Dechristé and L. Mieussens. A Cartesian cut cell method for rarefied flow simulations around moving obstacles. *Journal of Computational Physics*, 314:465–488, June 2016.
- [13] Jung Hee Seo and Rajat Mittal. A sharp-interface immersed boundary method with improved mass conservation and reduced spurious pressure oscillations. *Journal of Computational Physics*, 230(19):7347–7363, August 2011.

- [14] Lennart Schneiders, Daniel Hartmann, Matthias Meinke, and Wolfgang Schröder. An accurate moving boundary formulation in cut-cell methods. *Journal of Computational Physics*, 235:786–809, 2013.
- [15] Charles S Peskin. Flow patterns around heart valves: A numerical method. *Journal of Computational Physics*, 10(2):252–271, October 1972.
- [16] Markus Uhlmann. An immersed boundary method with direct forcing for the simulation of particulate flows. *Journal of computational physics*, 209(2):448–476, 2005.
- [17] Shen-Wei Su, Ming-Chih Lai, and Chao-An Lin. An immersed boundary technique for simulating complex flows with rigid boundary. *Computers & fluids*, 36(2):313–324, 2007.
- [18] Xiaolei Yang, Xing Zhang, Zhilin Li, and Guo-Wei He. A smoothing technique for discrete delta functions with application to immersed boundary method in moving boundary simulations. *Journal of Computational Physics*, 228(20):7821–7836, 2009.
- [19] E Arquis, Jean-Pierre Caltagirone, et al. Sur les conditions hydrodynamiques au voisinage d'une interface milieu fluide-milieu poreux: application à la convection naturelle. *CR Acad. Sci. Paris II*, 299(1), 1984.
- [20] Philippe Angot, Charles-Henri Bruneau, and Pierre Fabrie. A penalization method to take into account obstacles in incompressible viscous flows. *Numerische Mathematik*, 81(4):497–520, 1999.
- [21] Nicholas K-R Kevlahan and Jean-Michel Ghidaglia. Computation of turbulent flow past an array of cylinders using a spectral method with brinkman penalization. *European Journal of Mechanics-B/Fluids*, 20(3):333–350, 2001.
- [22] Randall J LeVeque and Zhilin Li. The immersed interface method for elliptic equations with discontinuous coefficients and singular sources. *SIAM Journal on Numerical Analysis*, 31(4):1019–1044, 1994.
- [23] Zhilin Li and Ming-Chih Lai. The immersed interface method for the navier–stokes equations with singular forces. *Journal of Computational Physics*, 171(2):822–842, 2001.
- [24] J Mohd-Yusof. For simulations of flow in complex geometries. *Annual research briefs*, 317:35, 1997.
- [25] Tao Ye, Rajat Mittal, HS Udaykumar, and Wei Shyy. An accurate cartesian grid method for viscous incompressible flows with complex immersed boundaries. *Journal of computational physics*, 156(2):209–240, 1999.
- [26] Ever A Fadlun, Roberto Verzicco, Paolo Orlandi, and Jamaludin Mohd-Yusof. Combined immersed-boundary finite-difference methods for three-dimensional complex flow simulations. *Journal of computational physics*, 161(1):35–60, 2000.

[27] Frederic Gibou, Ronald P Fedkiw, Li-Tien Cheng, and Myungjoo Kang. A second-order-accurate symmetric discretization of the poisson equation on irregular domains. *Journal of computational physics*, 176(1):205–227, 2002.

[28] Reza Ghias, Rajat Mittal, and Haibo Dong. A sharp interface immersed boundary method for compressible viscous flows. *Journal of Computational Physics*, 225(1):528–553, 2007.

[29] Mingshuo Han, Shiwei Hu, Tianbai Xiao, and Yonghao Zhang. A navier-stokes-peridynamics hybrid algorithm for the coupling of compressible flows and fracturing materials. *arXiv preprint arXiv:2504.11006*, 2025.

[30] Carlo Cercignani. *Rarefied gas dynamics: from basic concepts to actual calculations*, volume 21. Cambridge university press, 2000.

[31] Zhi-Gang Feng and Efthathios E Michaelides. The immersed boundary-lattice boltzmann method for solving fluid–particles interaction problems. *Journal of computational physics*, 195(2):602–628, 2004.

[32] Alexandre Dupuis, Philippe Chatelain, and Petros Koumoutsakos. An immersed boundary–lattice-boltzmann method for the simulation of the flow past an impulsively started cylinder. *Journal of Computational Physics*, 227(9):4486–4498, 2008.

[33] Jie Wu and Chang Shu. Implicit velocity correction-based immersed boundary–lattice boltzmann method and its applications. *Journal of Computational Physics*, 228(6):1963–1979, 2009.

[34] Luoding Zhu, Guowei He, Shizhao Wang, Laura Miller, Xing Zhang, Qian You, and Shiaofen Fang. An immersed boundary method based on the lattice boltzmann approach in three dimensions, with application. *Computers & Mathematics with Applications*, 61(12):3506–3518, 2011.

[35] Shin K Kang and Yassin A Hassan. A direct-forcing immersed boundary method for the thermal lattice boltzmann method. *Computers & Fluids*, 49(1):36–45, 2011.

[36] Julien Favier, Alistair Revell, and Alfredo Pinelli. A lattice boltzmann–immersed boundary method to simulate the fluid interaction with moving and slender flexible objects. *Journal of Computational Physics*, 261:145–161, 2014.

[37] Shi Tao, Haolong Zhang, Zhaoli Guo, and Lian-Ping Wang. A combined immersed boundary and discrete unified gas kinetic scheme for particle–fluid flows. *Journal of Computational Physics*, 375:498–518, December 2018.

[38] Lincheng Xu, Xu Yu, and Klaus Regenauer-Lieb. An immersed boundary-lattice boltzmann method for gaseous slip flow. *Physics of Fluids*, 32(1), 2020.

[39] Li Wang, John Young, and Fang-Bao Tian. An immersed boundary method for the thermo–fluid–structure interaction in rarefied gas flows. *Physics of Fluids*, 36(1), 2024.

[40] Cem Pekardan, Sruti Chigullapalli, Lin Sun, and Alina Alexeenko. Immersed boundary method for boltzmann model kinetic equations. In *AIP Conference Proceedings*, volume 1501, pages 358–365. American Institute of Physics, 2012.

[41] Lokesh Kumar Ragta, Balaji Srinivasan, and Sawan S. Sinha. Unified gas kinetic scheme combined with Cartesian grid method for intermediate Mach numbers. *International Journal for Numerical Methods in Fluids*, 85(9):507–524, November 2017.

[42] Prabhu Lal Bhatnagar, Eugene P Gross, and Max Krook. A model for collision processes in gases. i. small amplitude processes in charged and neutral one-component systems. *Physical review*, 94(3):511, 1954.

[43] Philip J Davis and Philip Rabinowitz. *Methods of numerical integration*. Courier Corporation, 2007.

[44] Tianbai Xiao. A flux reconstruction kinetic scheme for the boltzmann equation. *Journal of Computational Physics*, 447:110689, 2021.

[45] Yoshio Sone and Shigeru Takata. Discontinuity of the velocity distribution function in a rarefied gas around a convex body and the S layer at the bottom of the Knudsen layer. *Transport Theory and Statistical Physics*, 21(4-6):501–530, August 1992.

[46] Chanwoo Kim. Formation and Propagation of Discontinuity for Boltzmann Equation in Non-Convex Domains. *Communications in Mathematical Physics*, 308(3):641–701, December 2011.

[47] Yu-Heng Tseng and Joel H. Ferziger. A ghost-cell immersed boundary method for flow in complex geometry. *Journal of Computational Physics*, 192(2):593–623, December 2003.

[48] Mehrdad Yousefzadeh and Ilenia Battiat. High order ghost-cell immersed boundary method for generalized boundary conditions. *International Journal of Heat and Mass Transfer*, 137:585–598, July 2019.

[49] Graham W Alldredge, Martin Frank, and Cory D Hauck. A regularized entropy-based moment method for kinetic equations. *SIAM Journal on Applied Mathematics*, 79(5):1627–1653, 2019.

[50] Tianbai Xiao and Martin Frank. Relaxnet: A structure-preserving neural network to approximate the boltzmann collision operator. *Journal of Computational Physics*, 490:112317, 2023.

[51] Yoshio Sone. New kind of boundary layer over a convex solid boundary in a rarefied gas. *The Physics of Fluids*, 16(9):1422–1424, September 1973.

[52] Liyan Luo and Lei Wu. Multiscale simulation of rarefied gas dynamics via direct intermittent GSIS-DSMC coupling. *Advances in Aerodynamics*, 6(1), September 2024. Publisher: Springer Science and Business Media LLC.

[53] L M Yang, C Shu, J Wu, Y Y Liu, and X Shen. An efficient discrete velocity method with inner iteration for steady flows in all flow regimes. *Physics of Fluids*, 2024.

[54] Jianfeng Chen, Sha Liu, Rui Zhang, Congshan Zhuo, Yanguang Yang, and Chengwen Zhong. A global adaptive discretization of velocity space for discrete velocity methods in predictions of rarefied and multi-scale flows. *Physics of Fluids*, 36(8):086104, August 2024.

[55] Hongxu Chen, Christian Klingenberg, and Marlies Pirner. BGK model for rarefied gas in a bounded domain, February 2025. arXiv:2502.03096 [math].

[56] J.Y. Yang and J.C. Huang. Rarefied Flow Computations Using Nonlinear Model Boltzmann Equations. *Journal of Computational Physics*, 120(2):323–339, September 1995.

[57] Jing Fan, Iain D. Boyd, Chun-Pei Cai, Konstantinos Hennighausen, and Graham V. Candler. Computation of Rarefied Gas Flows Around a NACA 0012 Airfoil. *AIAA Journal*, 39(4):618–625, April 2001.

[58] Ahmad Shoja-Sani, Ehsan Roohi, Mohsen Kahrom, and Stefan Stefanov. Investigation of aerodynamic characteristics of rarefied flow around NACA 0012 airfoil using DSMC and NS solvers. *European Journal of Mechanics - B/Fluids*, 48:59–74, November 2014.

[59] Tianbai Xiao, Chang Liu, Kun Xu, and Qingdong Cai. A velocity-space adaptive unified gas kinetic scheme for continuum and rarefied flows. *Journal of Computational Physics*, 415:109535, 2020.

[60] Tianbai Xiao. Kinetic.jl: A portable finite volume toolbox for scientific and neural computing. *Journal of Open Source Software*, 6(62):3060, 2021.

[61] S. J. Plimpton, S. G. Moore, A. Borner, A. K. Stagg, T. P. Koehler, J. R. Torczynski, and M. A. Gallis. Direct simulation Monte Carlo on petaflop supercomputers and beyond. *Physics of Fluids*, 31(8):086101, August 2019.

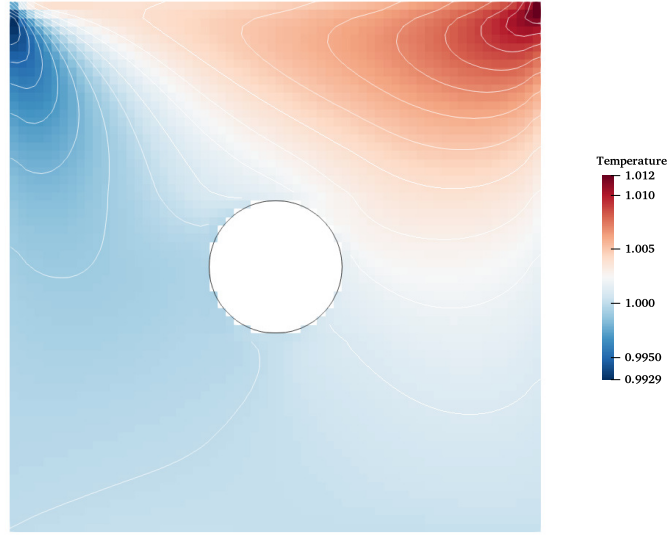


Figure 10: The converged temperature contour with the velocity space mesh of 200×200 .

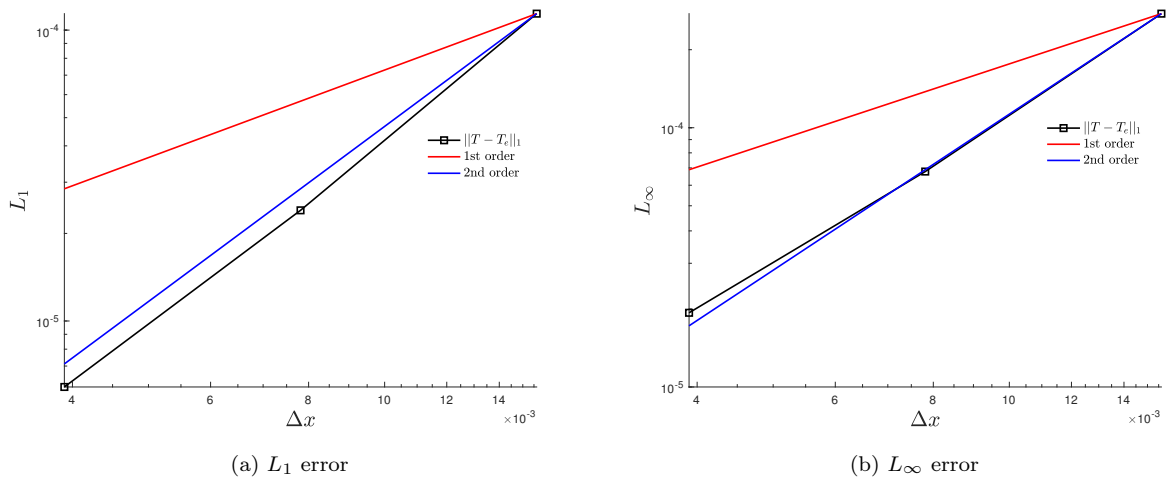


Figure 11: The variation of errors with physical mesh resolution, which validates the second-order convergence of the solution algorithm in the lid-driven cavity flow.

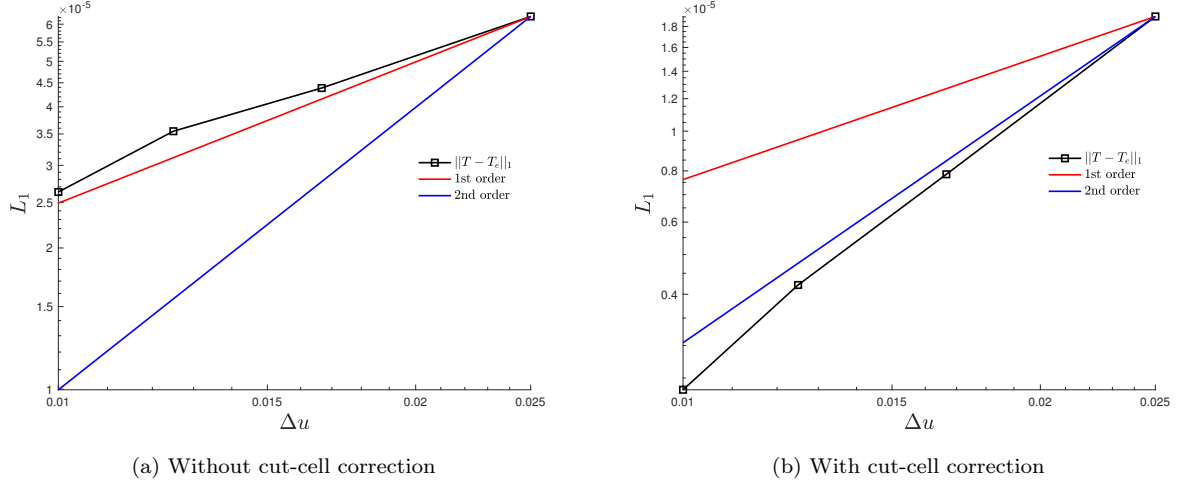


Figure 12: The comparison of the variation of L_1 error with velocity space mesh resolution with and without the cut-cell correction in velocity space in the lid-driven cavity flow.

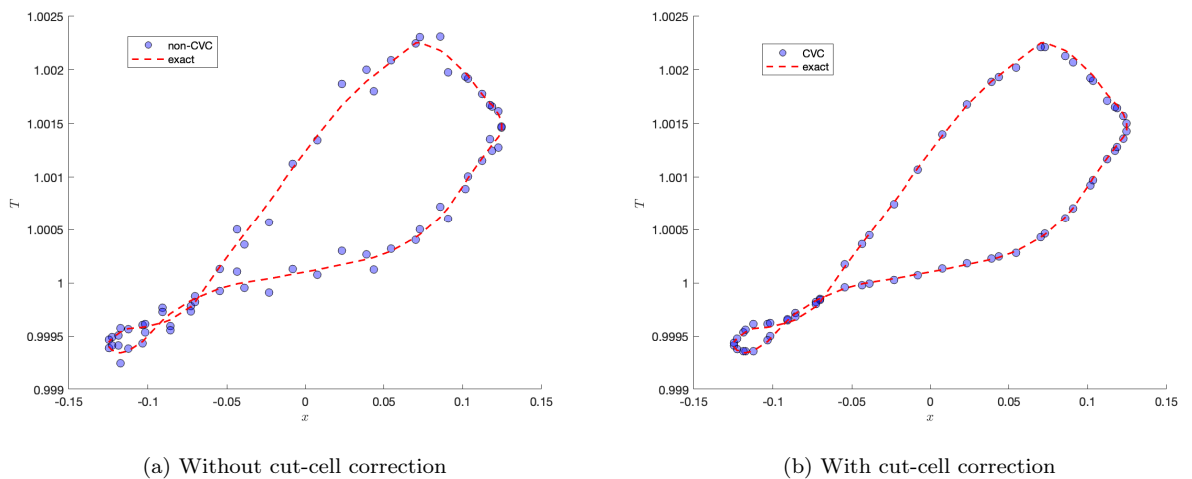


Figure 13: The comparison of cylinder surface temperatures with and without the cut-cell method using the same velocity mesh number of 40×40 in the lid-driven cavity flow.

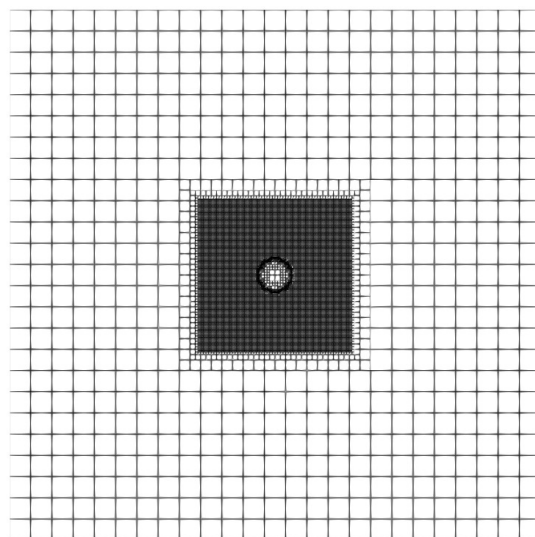
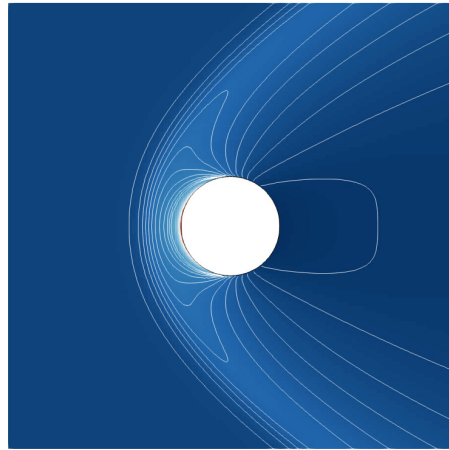
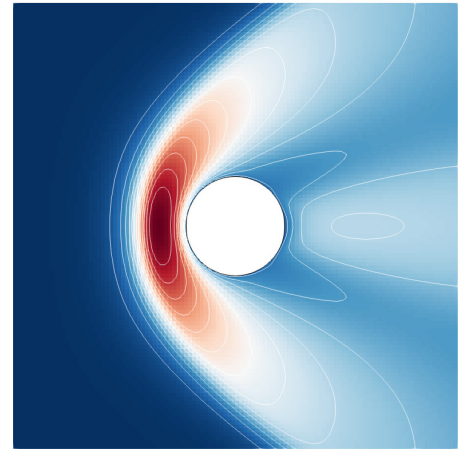


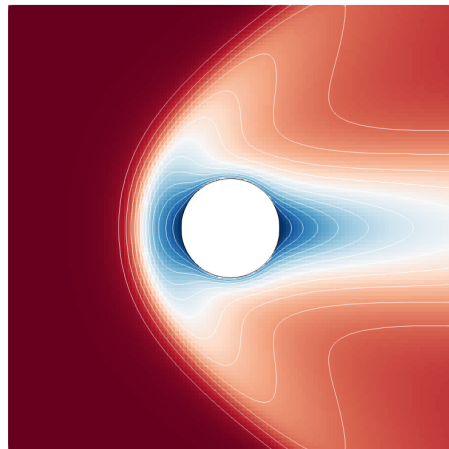
Figure 14: The physical mesh used for simulating the hypersonic flow around the cylinder.



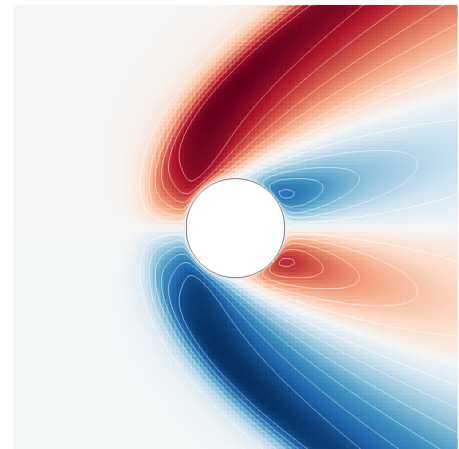
(a) Density



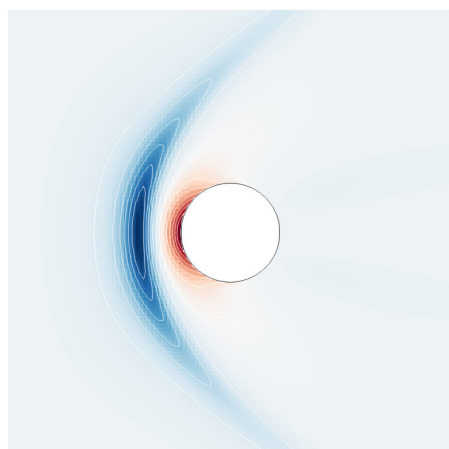
(b) Temperature



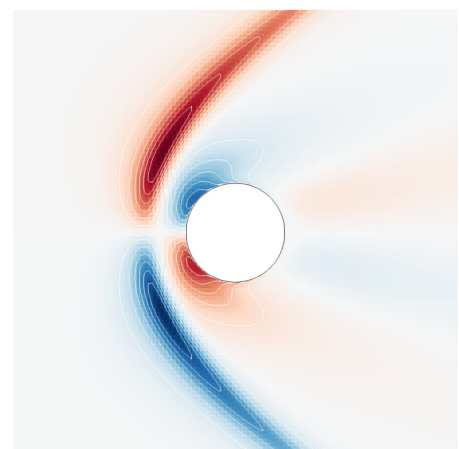
(c) X-component of velocity



(d) Y-component of velocity

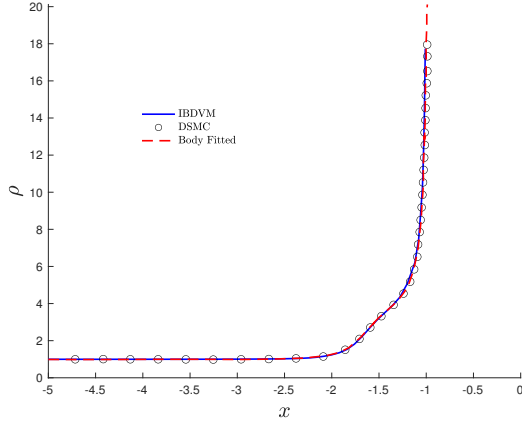


(e) X-component of heat flux

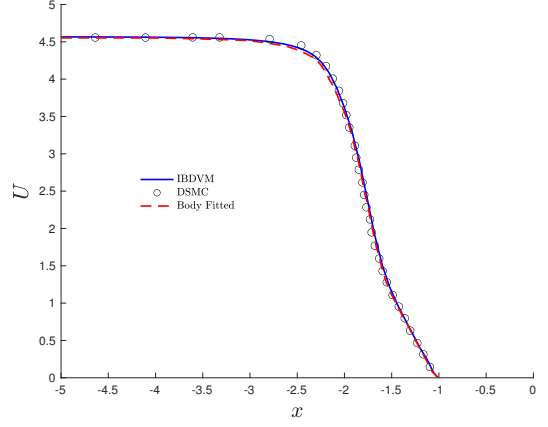


(f) Y-component of heat flux

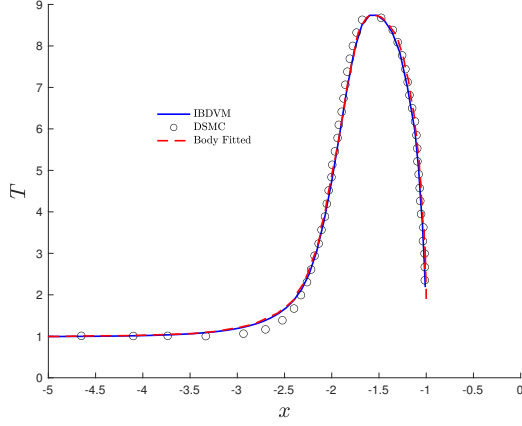
Figure 15: The converged contours of macroscopic flow variables in the hypersonic flow around the cylinder.



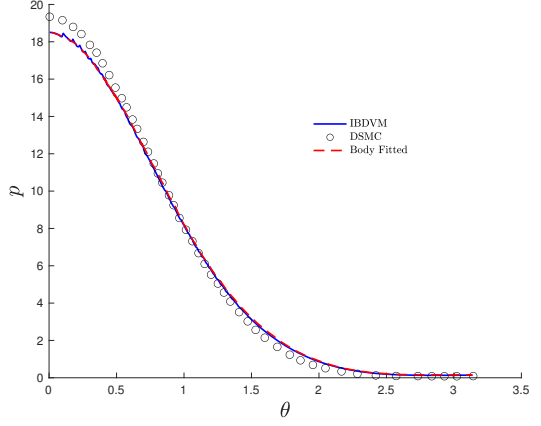
(a) Density along the stagnation line



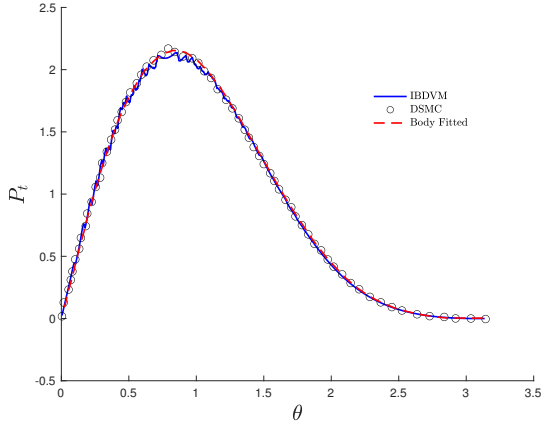
(b) X-component velocity along the stagnation line



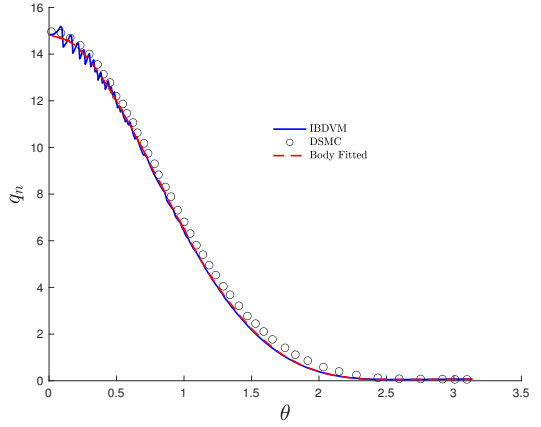
(c) Temperature along the stagnation line



(d) Pressure along the surface of the cylinder



(e) Shear stress along the surface of the cylinder



(f) Normal heat flux along the surface of the cylinder

Figure 16: The distribution of macroscopic flow variables along the stagnation line and surface of the cylinder in the hypersonic flow around the cylinder. The reference results of DSMC and the body-conformal DVM solver are extracted from [53].

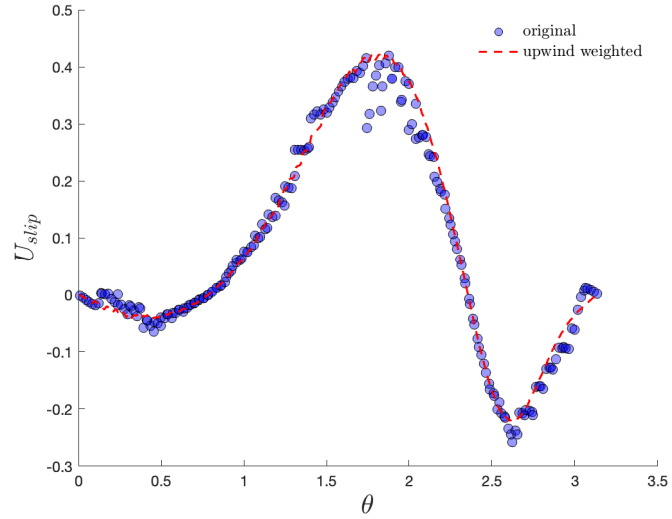


Figure 17: The comparison of slip velocity along the cylinder surface with and without the upwind-weighted interpolation method using the same physical mesh in the hypersonic flow around the cylinder.

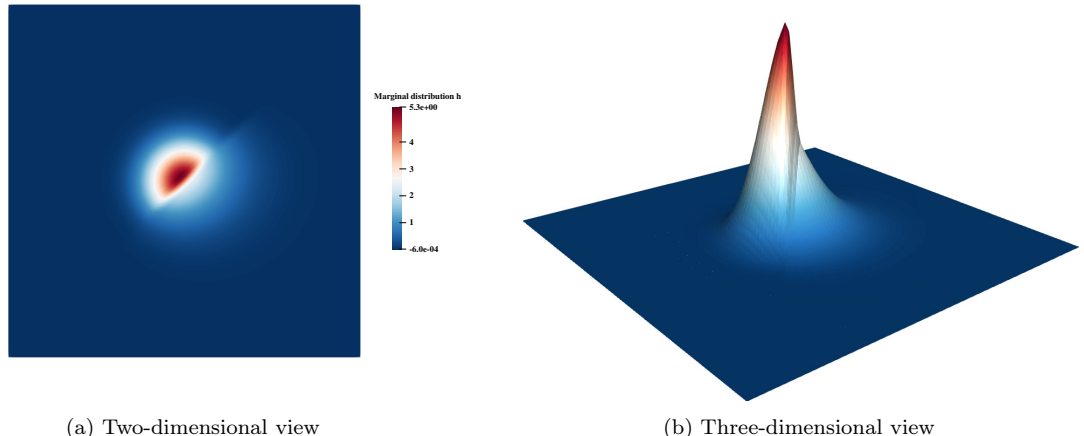


Figure 18: The particle distribution function in velocity space at $\theta = \frac{\pi}{4}$ on the cylindrical surface.

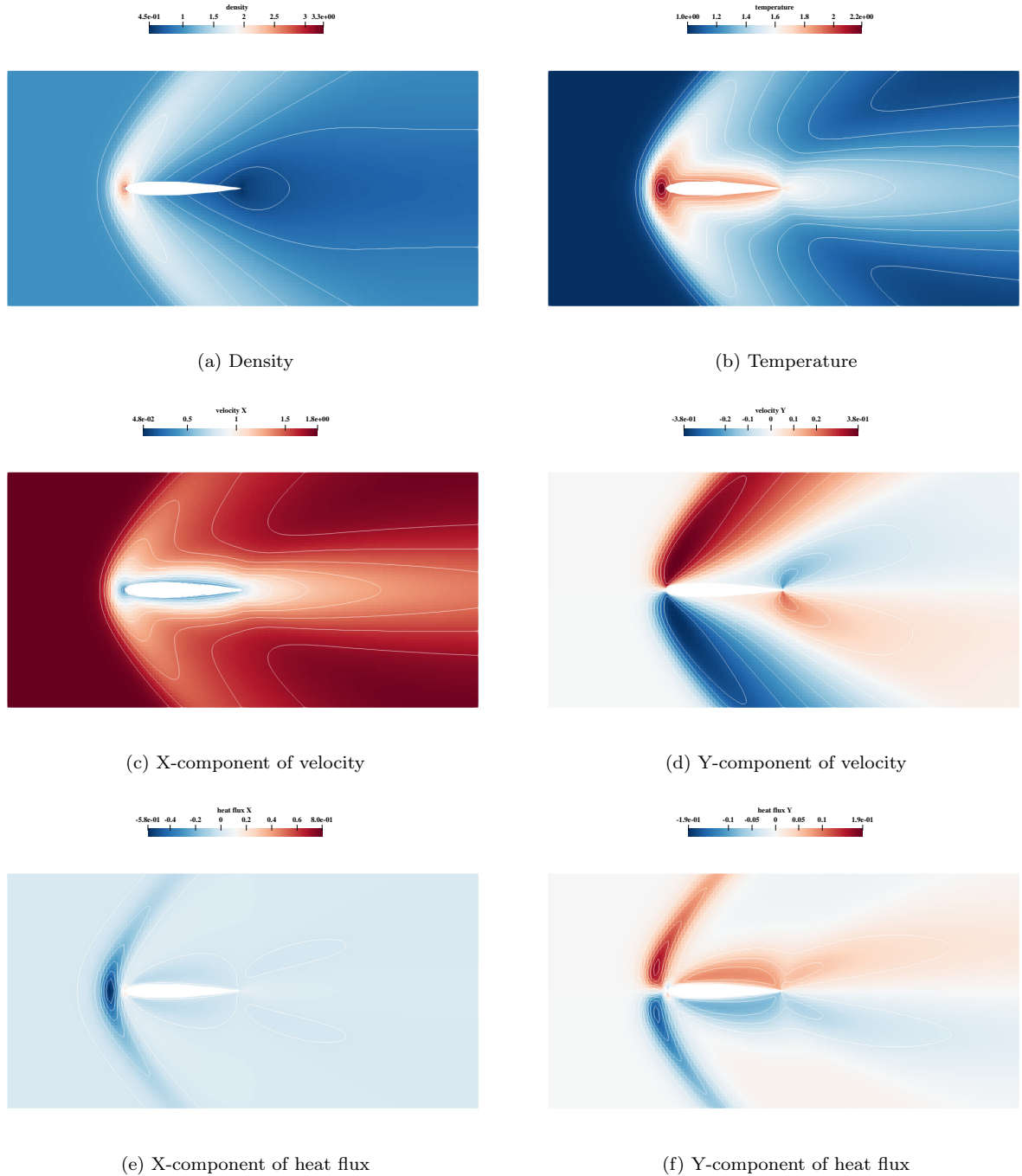
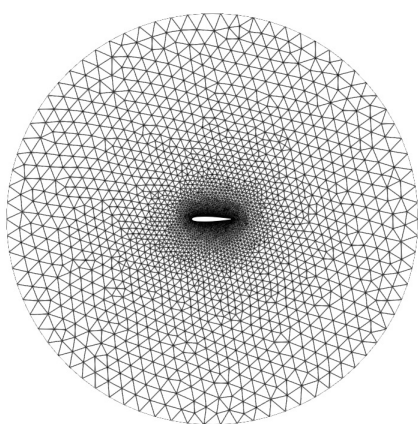
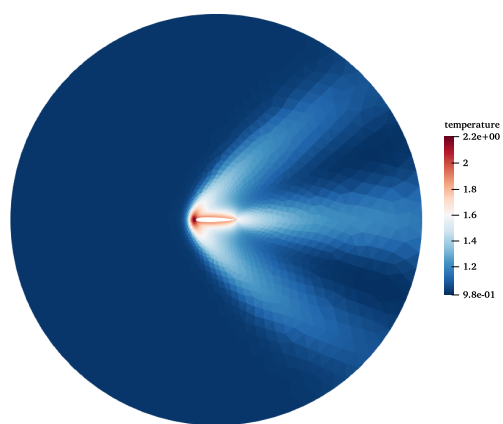


Figure 19: The converged contours of macroscopic flow variables in the supersonic flow around the NACA0012 airfoil.



(a) Unstructured mesh



(b) Temperature

Figure 20: The unstructured mesh and benchmark temperature contour used for validation in the supersonic flow around the NACA0012 airfoil.

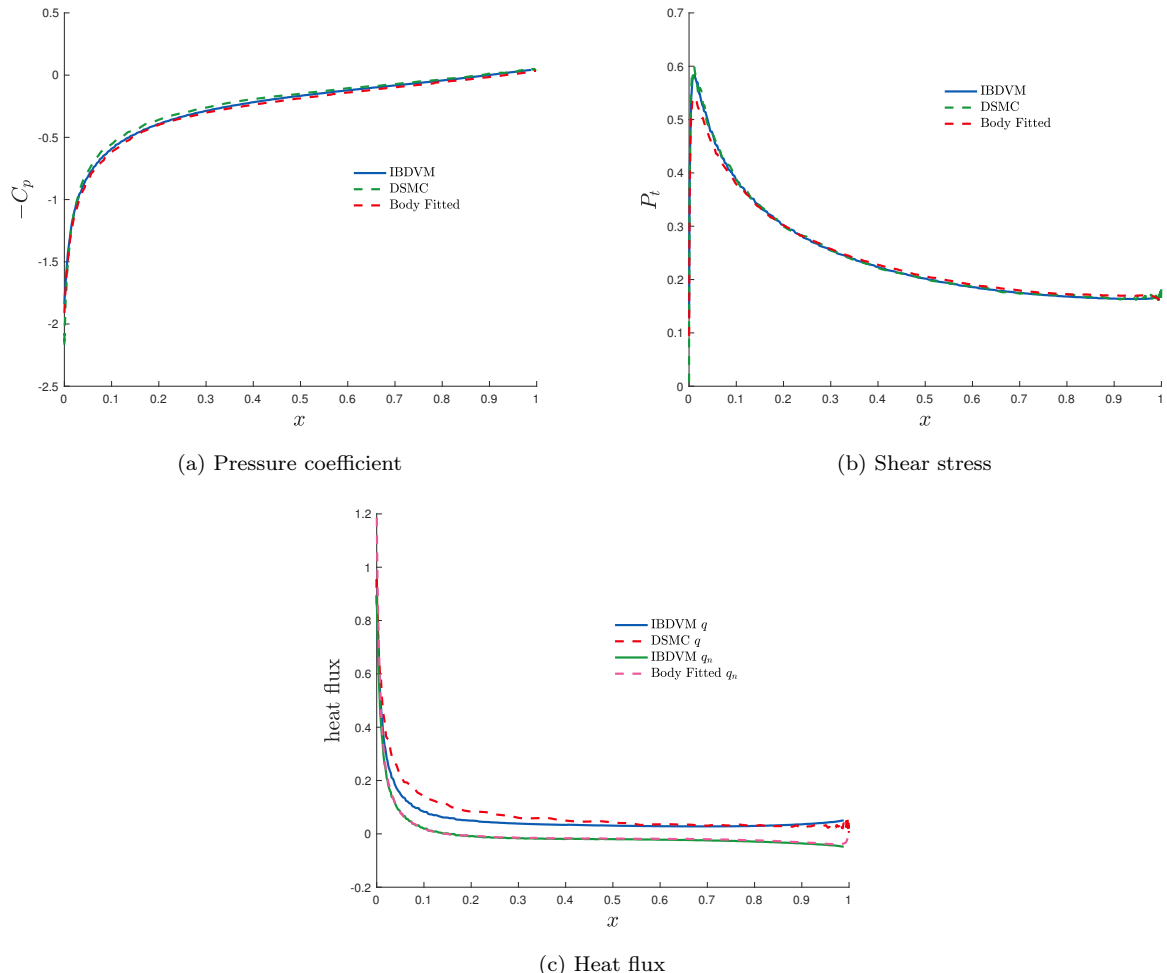
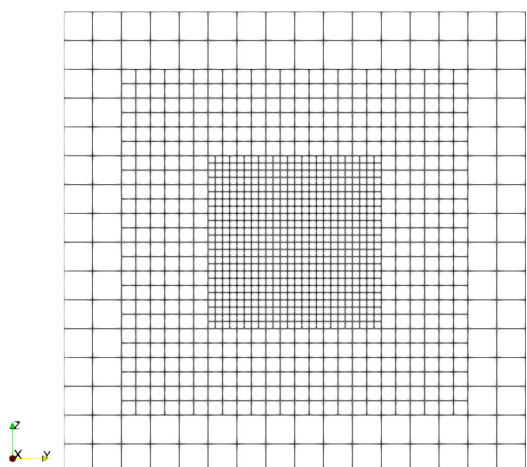
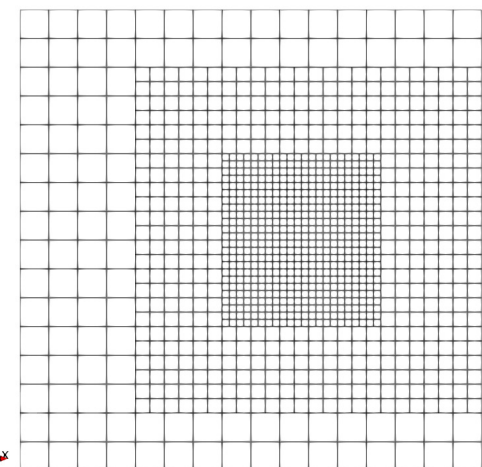


Figure 21: The comparison of macroscopic flow variables on the airfoil surface with the results simulated by DSMC and body-conformal DVM solvers in the supersonic flow around the NACA0012 airfoil.

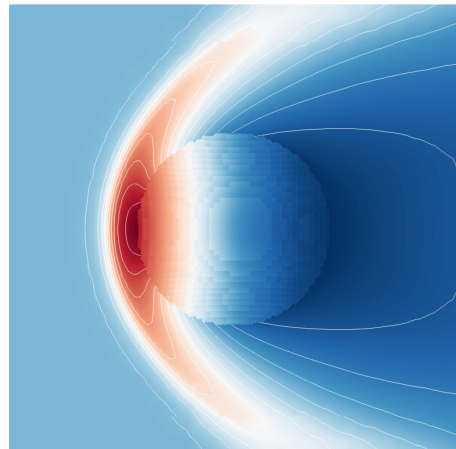


(a) Cross-section of the velocity space mesh at $x = 0$

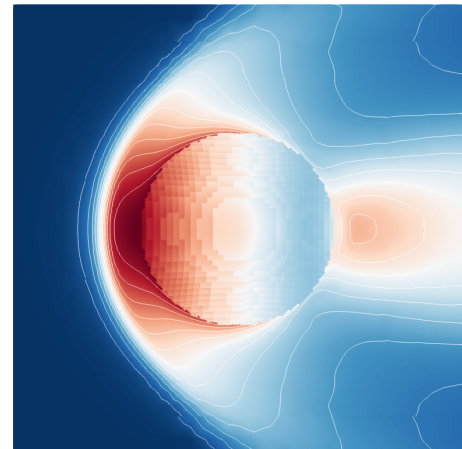


(b) Cross-section of the velocity space mesh at $z = 0$

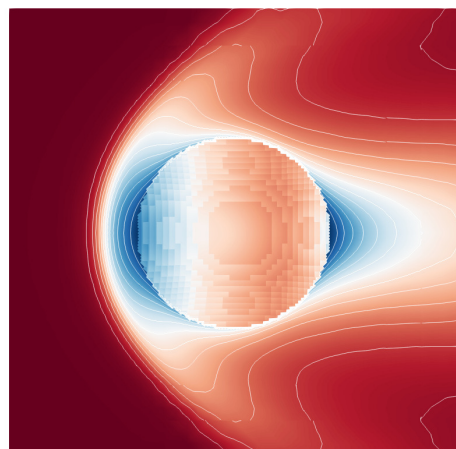
Figure 22: The velocity space mesh used in the supersonic flow around the sphere.



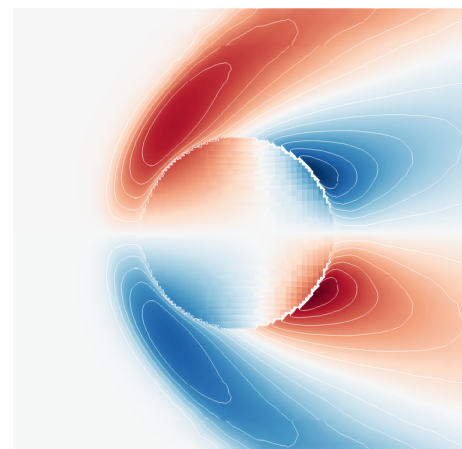
(a) Density



(b) Temperature



(c) X-component of velocity



(d) Z-component of velocity

Figure 23: The converged contours of macroscopic flow variables in the supersonic flow around the sphere.

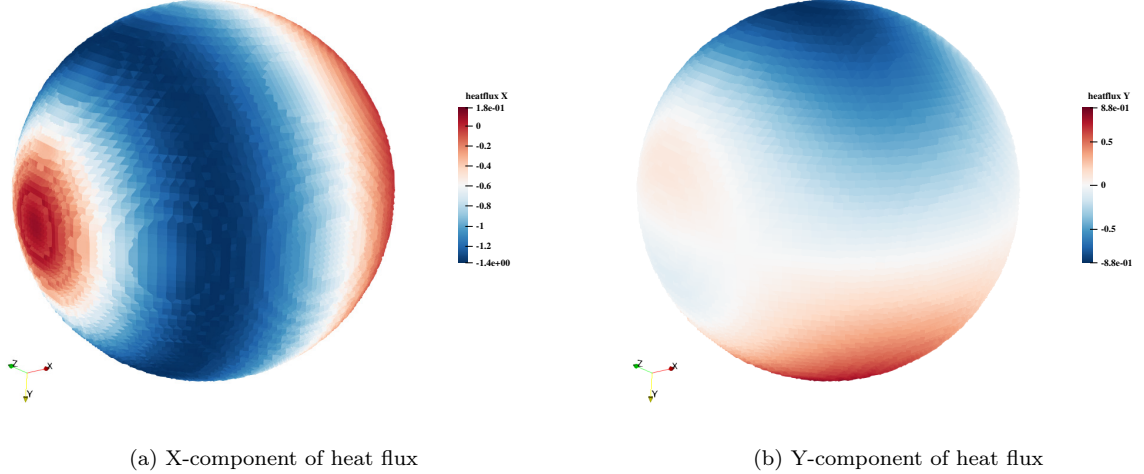


Figure 24: The heat flux near the surface in the supersonic flow around the sphere.

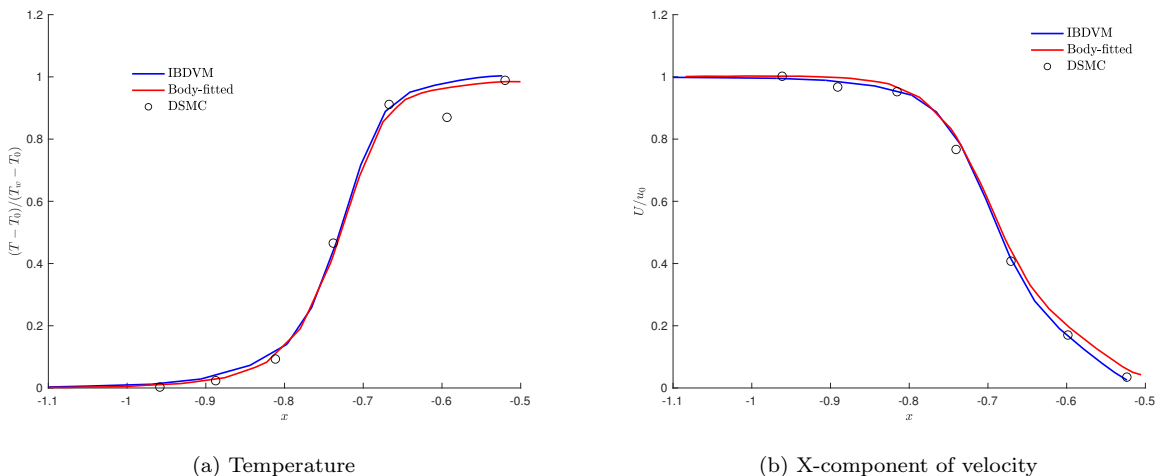


Figure 25: The distribution of macroscopic flow variables along the stagnation line in the supersonic flow around the sphere. The reference results of DSMC and the body-conformal DVM solver are extracted from [53].